CHALMERS
UNIVERSITY OF TECHNOLOGY

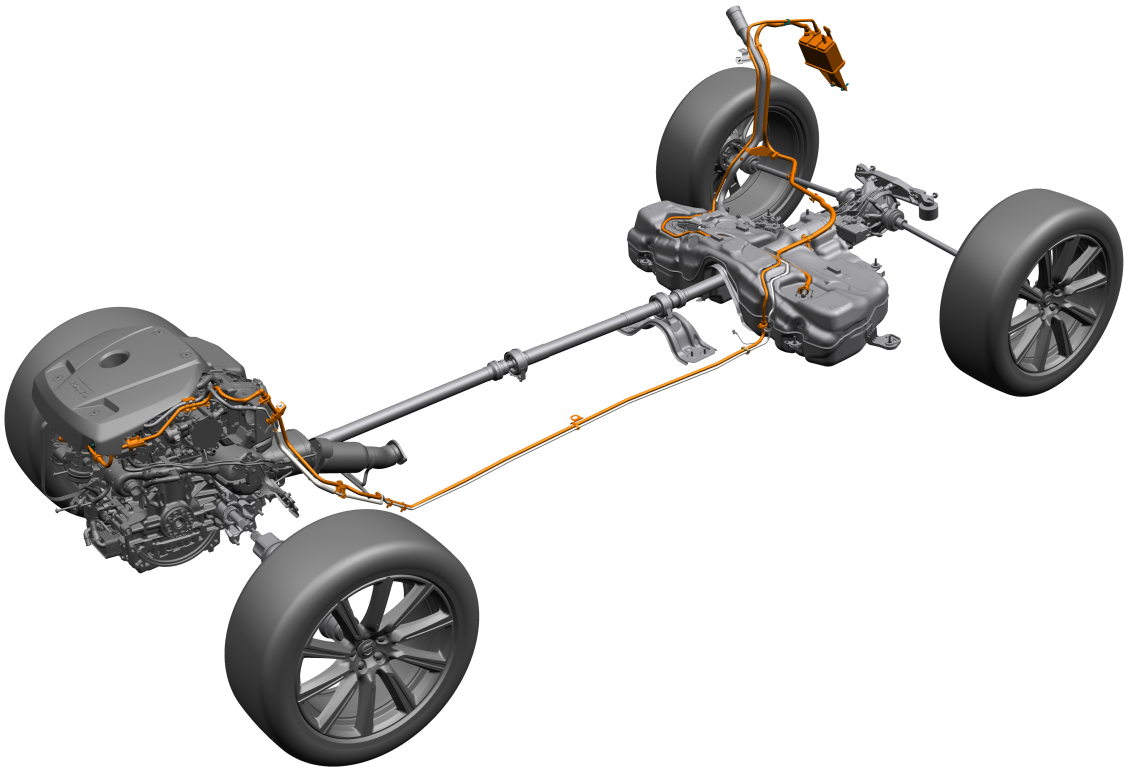

Modelling and Simulation of an Activated Carbon Canister

Non-isothermal transient 1D CFD simulations of adsorption and desorption of hydrocarbons onto activated carbon

Master's Thesis in Sustainable Energy Systems

ERIK MÖLLER

Department of Chemistry and Chemical Engineering
CHALMERS UNIVERSITY OF TECHNOLOGY
Gothenburg, Sweden 2016

Master's thesis 2016

Modelling and Simulation of an Activated Carbon Canister

Non-isothermal transient 1D CFD simulations of adsorption and desorption of hydrocarbons onto activated carbon

ERIK MÖLLER

CHALMERS
UNIVERSITY OF TECHNOLOGY

Department of Chemistry and Chemical Engineering
Division of Chemical Engineering
Chalmers University of Technology
Gothenburg, Sweden 2016

Modelling and Simulation of an Activated Carbon Canister
Non-isothermal transient 1D CFD simulations of adsorption and desorption of hydrocarbons onto activated carbon
ERIK MÖLLER

Supervisor: Christoffer Källerman, Volvo Cars
Examiner: Derek Creaser, Department of Chemistry and Chemical Engineering

Master's Thesis 2016
Department of Chemistry and Chemical Engineering
Division of Chemical Engineering
Chalmers University of Technology
SE-412 96 Gothenburg
Telephone +46 31 772 1000

Cover: The carbon canister highlighted in the car, as well as lines to the engine and the fuel tank.

Typeset in LaTeX
Gothenburg, Sweden 2016

Modelling and Simulation of an Activated Carbon Canister
Non-isothermal transient 1D CFD simulations of adsorption and desorption of hydrocarbons onto activated carbon
ERIK MÖLLER
Department of Chemistry and Chemical Engineering
Chalmers University of Technology

Abstract

The activated carbon canister is designed to adsorb and desorb dangerous volatile organic compounds evaporated from gasoline in a cars fuel tank. A simple cylindrical canister was built with a bed of activated carbon where loading and purging experiments were carried out measuring temperatures and the canister weight change.

A one dimensional CFD model was developed which predicts the experiments well. A comparison between a Langmuir adsorption model and the advanced Dubinin-Astakhov isotherm using a Linear Driving Force model where made where the later preforms better.

Using the 1D CFD model, a sensitivity analysis was done regarding length/diameter ratio, increased internal heat transfer, increased external heat transfer as well as an increased temperature of the purge flow. Only the increase in temperature of the purge flow shows a significant change in performance.

The non-isothermal behaviour of the canister shows the importance and difficulties to remove heat from the canister in order to maximize the capacity of the activated carbon.

The theoretical basis and the models developed in this thesis can be used to simulate simple non-isothermic loading and purging events for an ideal canister. The knowledge can be used as a foundation for more advanced 2D/3D models in the future, as well as input on how to efficiently construct a canister.

Keywords: Hydrocarbon adsorption, Activated carbon, Carbon canister, 1D CFD, GT-Suite, Dubinin-Astakhov isotherm, Langmuir adsorption model, LDF model.

Acknowledgements

This thesis is the result of my Master's Thesis project carried out at Volvo Cars in the spring of 2016. I would like to send a special thanks to my supervisor at Volvo Cars, Christoffer Källerman as well as Göran Fredriksson, Product Manager for the Carbon Canister at Volvo Cars. Your support and encouragement for this thesis have been much appreciated. A big thanks to my examiner at Chalmers, Derek Creaser, for valuable feedback.

Thank you Sofia Frändberg for providing me with valuable instructions and the application needed for the continuous balance logging. It has been a pleasure having you as a friend and thesis partner at Volvo with interesting discussions, lunching, and chitchat.

I would also like to thank all the other wonderful people at Volvo Cars who have helped and supported me throughout my thesis.

Erik Möller, Gothenburg, June 2016

Contents

List of Figures **xiii**

List of Tables **xv**

1 Introduction **1**
1.1 Background . . . 2
1.2 Purpose and objectives . . . 2
1.3 Demarcations . . . 3
1.4 Method . . . 3
1.5 Report structure . . . 3

2 Theory **5**
2.1 A brief overview of the carbon canister . . . 5
2.1.1 Loading . . . 6
2.1.2 Purging . . . 6
2.2 Activated carbon and adsorption . . . 7
2.2.1 Heterogeneous adsorption and physisorption . . . 7
2.2.2 Pore sizes and mass transport . . . 8
2.2.3 Heat of adsorption and thermal properties . . . 8
2.3 Adsorption equilibrium and kinetics . . . 9
2.3.1 The Langmuir isotherm . . . 9
2.3.2 Polanyi's potential theory of adsorption and the Dubinin-Astakhov isotherm . . . 11
2.3.2.1 The Dubinin-Astakhov isotherm equation . . . 12
2.3.2.2 Tuning the Dubinin-Astakhov isotherm . . . 13
2.3.3 Kinetics and the linear driving force . . . 13
2.4 Breakthrough and bleed emissions . . . 14
2.4.1 Breakthrough . . . 14
2.4.2 Diffusion and bleed emissions . . . 15
2.5 CFD calculations and 1D-models . . . 15
2.5.1 Equations solved in GT-Suite . . . 16
2.6 Literature review . . . 17
2.6.1 Modelling and simulation of hydrocarbon adsorption on activated carbon . . . 18
2.6.2 Canister design studies . . . 18
2.6.3 What is different in this thesis? . . . 19

3 Experimental methods **21**
3.1 Experimental setup and canister geometry . . . 21
3.1.1 Canister geometry . . . 21
3.1.2 Pressure drop connections and thermocouples . . . 22
3.1.3 Experimental setup . . . 22
3.2 Experiments and tests . . . 23
3.2.1 Pressure drop . . . 23
3.2.2 Loading . . . 24
3.2.3 Purging . . . 25
3.2.4 Canister orientation . . . 25

4 Simulation methods **27**
4.1 Solver settings . . . 27
4.2 Objects and project map . . . 27
4.2.1 The `CatalystBrick` object . . . 28
4.2.2 The `SurfaceReactions` object . . . 29
4.2.2.1 The Langmuir reaction . . . 29
4.2.2.2 The Dubinin-Astakhov LDF model . . . 30
4.3 Initial conditions and boundary conditions . . . 30
4.4 Loading and purging simulations . . . 31
4.5 Sensitivity analysis simulations . . . 31
4.5.1 Benefits, cost of change and response variables . . . 31
4.5.2 Parameters to be varied . . . 32
4.6 Optimization . . . 33

5 Results and discussion **35**
5.1 Experimental results . . . 35
5.1.1 Pressure drop . . . 35
5.1.2 Canister mass of the loading events . . . 36
5.1.3 Canister mass of the purging events . . . 36
5.1.4 Cumulative loading and purging . . . 37
5.1.5 Temperature measurements for a loading event . . . 38
5.1.6 Temperature measurements for a purging event . . . 39
5.1.7 Can radial heat transfer be neglected? . . . 40
5.1.8 Canister orientation . . . 41
5.1.9 Measurement errors and inaccuracies . . . 42
5.2 Simulations and comparisons with experimental results . . . 43
5.2.1 Pressure drop optimization . . . 43
5.2.2 Chemical reaction optimization . . . 43
5.2.2.1 The Langmuir isotherm . . . 44
5.2.2.2 The Dubinin-Astakhov isotherm . . . 44
5.2.2.3 Choosing the isotherm equation for simulations . . . 46
5.2.3 Loading . . . 46
5.2.4 Purging . . . 48
5.3 Sensitivity analysis . . . 49
5.3.1 Length/Diameter ratio . . . 49
5.3.2 Heating of purge gases . . . 50

5.3.3 Increased Internal and external heat transfer 50
5.3.4 Discretization length 51
5.4 The LDF time constant, internal mass transport and non constant purge flow 51

6 Conclusions and future work **55**

Bibliography **57**

A Canister geometry **I**

B Temperature sensors positions **III**

List of Figures

1.1 Sketch of a simple activated carbon canister seen from the side 2

2.1 A canister in a car, with lines to the fuel tank and the engine. 5
2.2 Approximate flow field inside a canister 6
2.3 Pore size distribution 8
2.4 Characteristics of an isotherm with regard to temperature and concentration 9
2.5 The characteristics of the Langmuir isotherm. 10
2.6 Equipotential surfaces $\varepsilon(W)$ between the gas film and the adsorbent . 11
2.7 The characteristic curve for an arbitrary adsorbate-adsorbent system 11
2.8 The Dubinin-Astakhov isotherm characteristics with a fixed adsorption potential 12
2.9 The canister mass and cumulative breakthrough for an ideal and a non-ideal canister 14
2.10 Discretization of a plug flow reactor 15

3.1 Geometry of the experimental canisters 21
3.2 The temperature sensor positions for canister 1. 22
3.3 Exprimental setup during loading events 23
3.4 Experimental setup of the pressure drop measurements 24
3.5 The different orientations of the canister, with gravity vectors plotted 25

4.1 The canister subassembly in GT-Suite. 28

5.1 The pressure drop over the carbon bed for the two canisters. 35
5.2 The canister mass gain for the loading events 36
5.3 The canister mass loss for the purging events 37
5.4 Canister mass gain/loss with regard to the cumulative flow. 38
5.5 Mass gain and temperatures for loading case D 38
5.6 Temperature in the center of the canister, and the mass loss, for purge case B 39
5.7 Thermocouples normalized position for measuring radial heat transfer 40
5.8 Temperatures at the same axial position for the loading and purging event. 40
5.9 The loading event with a vertical and horizontal canister with labeled temperature position 41

5.10 Balance recording of a loading experiment without any adjustments or filtering. 42
5.11 Simulation of the pressure drop along the experimental results 43
5.12 Langmuir isotherm equation fitting 44
5.13 Dubinin-Astakhov isotherm equation fitting 45
5.14 A comparison between the measured data, the Langmuir model and the Dubinin-Astakhov LDF model 46
5.15 Simulation of the loading experiments 47
5.16 Simulation and measurements of the temperature and weight gain during case B loading experiment. 47
5.17 Simulation of the purging experiments 48
5.18 Simulation and measurements of purge case B. 48
5.19 The simulated sensitivity analysis with respect to different length/-diameter ratios. 49
5.20 Simulation of a purging event using different incoming temperatures. 50
5.21 Sensitivity analysis of an increased internal and external heat transfer. 51
5.22 The influence of changing the LDF time constant 52
5.23 Simulation of a purging event with varying flow rate. 52
5.24 Simulation of a nonconstant purging event with different LDF time constants. 53

A.1 Detailed sketch and measurements of the canister geometry I

List of Tables

3.1 Loading experiments 24
3.2 Purging experiments 25

4.1 The geometry properties for the `CatalystBrick` object 28
4.2 The Detailed Wall Layer Geometry and Temperature Solver object used for the `CatalystBrick` object 29
4.3 Simulations of loading experiments 31
4.4 Simulations of purging experiments 31
4.5 Sensitivity analysis of the length/diameter ratio 32

5.1 Loading experiments 36
5.2 Purging experiments 37
5.3 The parameters used for the Langmuir isotherm fitting 44
5.4 Parameters found for the Dubinin-Astakhov isotherm 45
5.5 Simulation of the average pressure drop over the canister using a constant purging flow. 49
5.6 Simulation of the purging time using a constant purging flow. 50

B.1 Temperature sensors positions for experimental canister 1. III
B.2 Temperature sensors positions for experimental canister 2. IV

1
Introduction

When one thinks about emissions from cars and the automotive industry, there is a lot of focus on tailpipe emissions such as CO_2 and NO_x. This work focuses on another type of emission, which is called the evaporative emissions, where the causes of emissions are from the fuel storage and refueling process.

Gasoline is a fuel mix which contains a lot of different types of hydrocarbons, both light ones and heavy ones. The light ones like butane and pentane are volatile and are likely to evaporate from the liquid gasoline to a gas phase in the fuel tank.

The gas phase with the volatile organic compounds (VOCs) can be exposed to increased pressure in the fuel tank due to two different phenomena. The first phenomenon takes place when the temperature of the fuel tank rises and the second phenomenon happens when the car is refueled so that the gas phase must be compressed in order to make room for an increased liquid phase.

Because of safety reasons, the fuel tank should ideally not be pressurised. Therefore a simple solution would be to connect the fuel tank to the surrounding atmosphere so that an atmospheric pressure is always present in the fuel tank. The VOCs are however dangerous to human and nature and should therefore not be released to the surroundings. To solve this problem, car manufacturers install an active carbon canister which is connected in between the fuel tank and the atmosphere.

The carbon canister adsorbs the VOCs onto the activated carbon so that only clean air is released to the surroundings. The activated carbon does however have a limited capacity which means that the canister must be purged regularly in order to function well. The purging process means that clean air is being pulled in through the canister, which desorbs the VOCs from the activated carbon, and the air/VOCs mixture is fed to the engine where it is combusted. This means that the canister both reduces the evaporate emissions and also improves fuel economy since the fuel is used in the engine rather than being wasted.

Even though the canisters have existed for a long time, the solution to stricter regulations have been countered with larger canisters and better activated carbon. The transition towards electromobility have however introduced hybrid vehicles where the electric drive and internal combustion engine can work together, or separately, which creates new conditions for the canister. A hybrid vehicle's fuel tank can be exposed to the same phenomena as a conventional gasoline powered car which means that the canister loading in a hybrid vehicle can look familiar. The purging process can however be extremely limited due to the fact that the hybrid vehicle might not even start the internal combustion engine at all for shorter trips. This creates a new demand for canisters which are as efficient as possible, and the knowledge for how to achieve this.

1.1 Background

Derwent (1995) describes the historical background about the danger with VOCs in the atmosphere, where the earliest work was carried out in the mid 1950s in the light of Los Angeles smog. The hazard of smog gradually led to stricter regulations for the evaporative emissions which made the automotive industry try to adapt.

Johnson, Setsuda, and Williams (1999, p. 237) reports that the first carbon canister was installed after California regulations in the early 1970s. The first patent for an active carbon canister is filed by Hall (1965) and even though the patent is using a slightly different purging technique, the canisters today work in a similar way as when they were invented over 50 years ago.

The carbon canister is the main subject of this thesis. It consist of a plastic housing filled with a bed of activated carbon which can adsorb hydrocarbons. It is connected to the atmosphere on one side and has two connections on the other side, one connection from the fuel tank and one connection into the engine. Figure 1.1 shows the geometry of a canister where all connections are conveniently put on the same side and a solid wall separates the connections and creates a long adsorption zone in between. The dotted area in the figure represent the volume filled with activated carbon. Note that the geometry and flow patterns might not be ideal in a real world canister due to the fact that it must be compact, be simple to manufacture, and connections should be easy to mount.

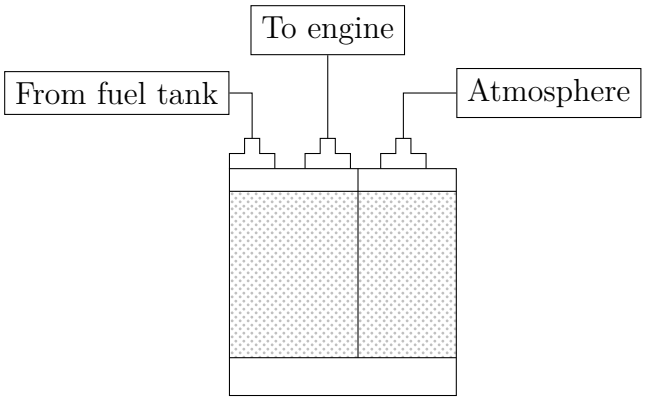

Figure 1.1: Sketch of a simple activated carbon canister seen from the side

1.2 Purpose and objectives

The purpose of this thesis is to develop a simulation method to be able to predict adsorption and desorption of hydrocarbons in an activated carbon canister. This is of importance because the automotive industry can save time and money by having more simulations and fewer physical tests.

The goal for this project is to determine if it is possible to accurately predict the adsorption and desorption process for an ideal canister where the flow pattern is close to ideal. The methods and results in this thesis could then be used to tell if a real carbon canister works as planned or if there are problems with the canister,

such as dead zones or bypass channels within the active carbon bed. The knowledge and results found in this project could also be used to simulate the current canisters for different design points and the knowledge could also be used as a foundation if a new canister would be designed.

1.3 Demarcations

This thesis will not do any experiments or testing on real canisters but rather try to develop a simulation model which works for an ideal case where geometry and flow fields do not heavily influence the solution.

1.4 Method

In order to predict the adsorption and desorption of VOCs the project consists of an experimental part and a modelling part. The experimental part consist of building and making tests on an exprimental active carbon canister. The modelling part consists of implementing chemical models which predicts the behaviour and properties of the canister, such as temperature and adsorption.

The model should be implemented in a computer aided engineering (CAE) application called GT-SUITE developed by Gamma Technologies, LLC. GT-SUITE is a 1D fluid field solver in which a lot of automotive applications could be simulated. Chemical surface reactions could be implemented by using an approach where a catalyst brick can be used to model the carbon bed either in 1D, 2D or even 3D.

The thesis is being carried out at the fuel system section of Volvo Cars. This section is responsible for components such as the fuel tank, the fuel pump, the refueling pipe, and the evaporative control system (EVAP system) in which the canister is a component.

1.5 Report structure

The report is divided into a theory chapter where the fundamental theory of hydrocarbon adsorption and its mechanisms are described. The report contains a chapter on the experimental setup and a chapter on experimental methods used to implement the simulation code. The results are presented and discussed before the last chapter which covers conclusions and further work. Additional information is found in the appendices.

2
Theory

The phenomena and mechanisms occurring in the activated carbon canister can be quantified over different scales, from the micro scale of individual atoms which bonds to the activated carbon surface, to the macro scale where the adsorption and desorption can be described with measures like temperature and concentration, to the largest mega scale where the interior of the canister is regarded as a black box.

2.1 A brief overview of the carbon canister

The activated carbon canister (also called *carbon canister* or just *canister*) is a relatively simple component which consists of a plastic housing, a carbon bed, some filters and protection in order to keep the carbon bed fixed, and lastly some connection nipples. The canister is connected to the atmosphere on one side of the carbon bed and connected to the fuel tank and engine on the other side of the carbon bed. Figure 2.1 shows a parts of a 2016 Volvo XC90 built for the nordic market. The canisters location in the car varies and in fig. 2.1 the canister is located over the right rear wheel. The lines from the fuel tank to the canister as well as the line from the canister to the engine are shown.

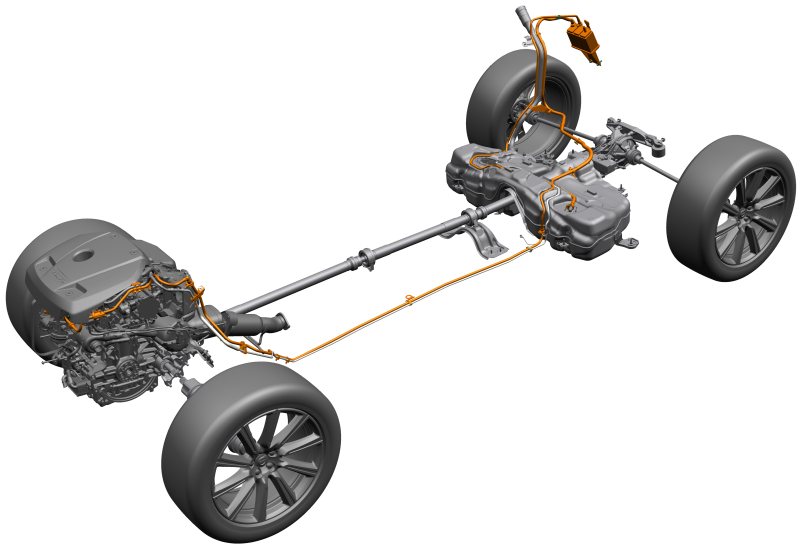

Figure 2.1: A canister in a car, with lines to the fuel tank and the engine.

The event where fuel vapors are adsorbed in the canister is called loading while the event of desorbing the fuel vapors is called purging. The approximate flows inside the canister for these events can be seen in fig. 2.2.

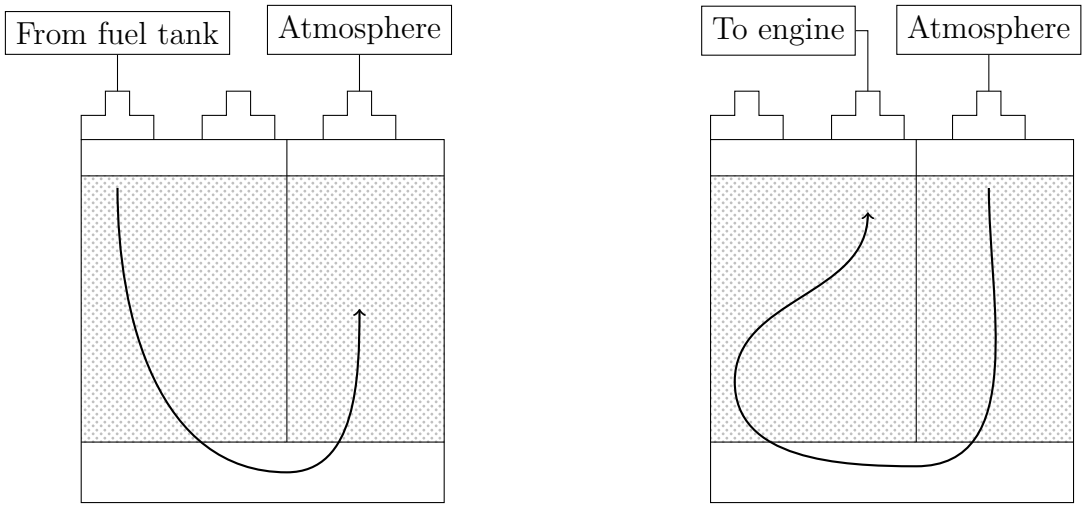

(a) Loading (b) Purging

Figure 2.2: Approximate flow field inside a canister

2.1.1 Loading

The loading event takes place because of either two different reasons.

Firstly, loading takes place when the ambient temperature rises around the fuel tank so that fuel vapors are evaporated. This is a slow loading event and thus the flow rates when this event takes place are only in the order of grams per hour.

Secondly, loading of the canister also takes place when the vehicle is refueled. The refueling event means that the fuel vapors are being pushed to the canister when liquid fuel fills up the volume of the fuel tank. Because the refueling event happens in the order of minutes, this event is very rapid and the flow rates are about two order of magnitude higher than the slow loading.

Some regulations, like in the US, require that the canister should be able to adsorb all fuel vapors in the case of refueling, which is called Onboard refueling vapor recovery (ORVR). In other markets there can be a system where the fuel pump itself takes care of the fuel vapors created so that the canister is not loaded as heavily as in ORVR. This also implies different canister sizes for different markets. Liu et al. (2015) says that canisters for US markets have 2-3 liters of activated carbon while the European ones have about 1 litre of carbon.

2.1.2 Purging

The event where hydrocarbons are desorbed from the carbon bed is called purging. This event only takes place when the engine is running by flowing air through the canister and putting the mixture of air and desorbed hydrocarbon in the air inlet of the engine.

The air is forced through by a low pressure side by the engine. This pressure varies over different driving conditions and thus the mass flow of air forced through the canister varies, but it is typically in the range of 10 to 100 litres of air per minute. The mass flow is further controlled by the purge valve and check valve which controls the flow and ensures that the flow is never reversed.

A low pressure drop over the canister is desired since a high pressure drop requires a large back pressure which must be created by the engine. Since the exploitation of an engine's back pressure reduces the efficiency of the engine, a high pressure drop over the canister increase the fuel consumption of the engine which also increases the CO_2-emissions.[1]

2.2 Activated carbon and adsorption

The canister is filled with a bed of activated carbon which adsorb hydrocarbons in the loading event and desorb hydrocarbons when purging. Activated carbon for automotive applications is usually produced in granulates or pellets in the size of a few millimeters. The carbon can be produced from biomass like wood or coconut shell as well as from bituminous coal. The raw material is mixed with a binder and then goes through different processes including high heat thermal treatment, conditioning, and pelletizing. When going through the processes the product become *activated* which means that the carbon become extremely porous and will have a very large surface area. (Johnson et al., 1999)

2.2.1 Heterogeneous adsorption and physisorption

The event of adsorption is described as when an *adsorbate* adsorbs onto an *adsorbent*. In this thesis the adsorbate consists of gaseous hydrocarbons while the adsorbent is the solid activated carbon. Since the adsorbate and adsorbent have different phases, this is called heterogeneous adsorption. (Bansal & Goyal, 2005, p. 67)

Adsorption could be seen as a very simple chemical reaction where the adsorbate X together with an vacant site from the adsorbent S form the adsorbed state SX:

$$\mathrm{X} + \mathrm{S} \longrightarrow \mathrm{SX} \tag{2.1}$$

For a *physisorption* event, a molecule X in the gas phase is by van der Waals forces bound to a vacant site S onto surface of the adsorbent. Van der Waals forces means that the bond exist because of induced, permanent or transient electric dipoles between the molecule and the surface of the adsorbent. Physisorption is a relatively weak interaction compared to the chemisorption event were the adsorbate and adsorbent interchange electrons. (Bansal & Goyal, 2005, p. 68)

[1] A low pressure drop is also desired since a refueling pump will automatically shut of if a too high pressure is created in the refueling pipe section, caused by a high pressure drop over the canister where the air/fuel vapors should escape.

2.2.2 Pore sizes and mass transport

There is a limited number of vacant sites where the adsorbate can bond, a high porosity and a large surface area are favourable in order to efficiently adsorb a large amount of the adsorbate. Figure 2.3 visualizes different pore sizes in activated carbon. These pores all have different roles in the adorption process. *A* refers to a macropore (>500 Å) which is the most inefficient pore size for adsorption, but the macropores does serve the purpose of transporting molecules to the smaller pores. *B* represent a mesopore (20-500 Å) which is the most important pore size for hydrocarbon adsorption since it can both efficiently adsorb molecules and easily release the molecules in the purging event. *C* is a micropore (<20 Å) which is very efficient for adsorption but too small for efficient desorption.

Since the mesopores are most efficient for adsorption and desorption of hydrocarbons, carbon used for automotive applications usually have a high fraction of these mesopores.

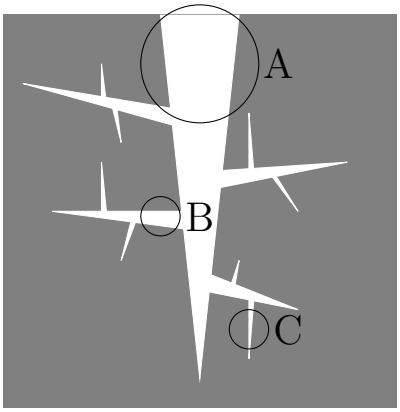

Figure 2.3: Pore size distribution

As stated by Knaebel (2008, p.1140), the event where the molecules are transported from the bulk into the pores of carbon is of great interest since it can limit the rate of adsorption and desorption. The mass transport from the surrounding film of the adsorbent into the mesopores consist of several mechanisms. This includes film diffusion through the film between bulk and particle, the diffusion through the macropores and the diffusion in the mesopores.

2.2.3 Heat of adsorption and thermal properties

Physisorption is always an exothermic event as described by Knaebel (2008, p. 1133). This means that the carbon bed will become heated during loading and cooled in the event of desorption during purging. Since temperature affects the previously discussed diffusion, a lot of coupled and simultaneous phenomenas will happen regarding heat and mass transfer. It should also be noted that low temperatures are favorable for high loading, which means that the exothermic heat release works against the loading, implying a negative feedback.

As the adsorption event progresses, more and more adsorbate will be bounded to the adsorbent. This means that the apparent density, as well as other thermal

properties, will change throughout the adsorption process. The change of these properties will increase the complexity in a mathematical model but can be avoided if a fixed average is used instead, at the cost of reduced accuracy.

2.3 Adsorption equilibrium and kinetics

A common concept when dealing with adsorption is the adsorption equilibrium. The equilibrium describes the loading of an adsorbate onto an adsorbent, and is usually expressed in units like grams of adsorbate per grams of adsorbent. The equilibrium for an adsorption process is strongly related to two parameters; the temperature and the partial pressure of the adsorbate, i.e. the concentration of the gaseous phase. The equilibrium does not contain any information about how fast the adsorption event occurs. (Knaebel, 2008, p. 1133)

The equilibrium of an adsorbate-adsorbent system is usually described as an isotherm. This means that the loading is expressed as a function of concentration of the gas composition, having a constant temperature. The fractional loading is usually denoted θ and defined as

$$\theta = \frac{\text{Amount adsorbed}}{\text{Maximum amount adsorbed}} \tag{2.2}$$

so that θ is unitless and can take any value between 0 and 1. If $\theta = 0$ it means that the system is empty and no adsorption has taken place while $\theta = 1$ means a fully saturated system where there is exactly no vacant sites available for further adsorption.

While an isotherm is more or less unique for the adsorbate-adsorbent system and can look very different, it usually follows that a lower temperature and a higher concentration yield a higher loading. This is visualized in fig. 2.4 where three different isotherms, each at a different fixed temperatures, are plotted against the partial pressure p_i of species i.

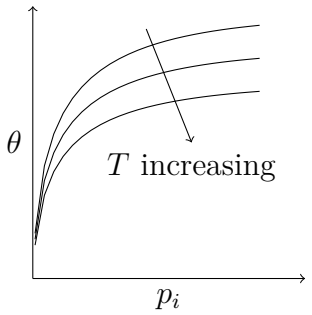

Figure 2.4: Characteristics of an isotherm with regard to temperature and concentration

2.3.1 The Langmuir isotherm

The Langmuir isotherm is one of the simplest isotherm with a number of assumptions regarding the adsorption process. The adsorbent surface is considered flat and

homogeneous so that each vacant site of the adsorbent surface will have the same probability of adsorbing an adsorbate molecule. The Langmuir isotherm further assume that the adsorbed molecule does not interact with any other molecule on the surface and that only one molecule could adsorb onto the same site.

With these assumptions, two rate expressions could be set up for the adsorption and desorption reaction for when a molecule X is adsorbing onto a vacant site S forming the adsorbed state SX:

$$\mathrm{S} + \mathrm{X} \underset{r_{des}}{\overset{r_{ads}}{\rightleftharpoons}} \mathrm{SX} \tag{2.3}$$

$$r_{ads} = k_{ads} p_i (1 - \theta) \tag{2.4}$$

$$r_{des} = k_{des} \exp(-E_A/(RT))\theta \tag{2.5}$$

where k_{ads} and k_{des} are reaction rate multipliers, p_i is the partial pressure (concentration) of species i, θ is the fractional local coverage, E_A is the activation energy, R is the universal gas constant, and T is the temperature.

Isotherms are expressed at equilibrium and the *net rate* of adsorption is zero at equilibrium. With $r_{ads} - r_{des} = 0$ and solving for θ yield the Langmuir isotherm. (Bansal & Goyal, 2005, pp 78-90)

$$\theta = \frac{bp_i}{1 + bp_i} \tag{2.6}$$

where the constant b is defined as

$$b = \frac{k_{ads}}{k_{des}} \exp(E_A/(RT)) \tag{2.7}$$

The simplicity and the scientific basis of the Langmuir isotherm has made it very popular. The isotherm only has two unknown variables, the ratio $\frac{k_{ads}}{k_{des}}$ and the activation energy E_A. The characteristics of a Langmuir isotherm is seen in fig. 2.5. As stated in section 2.3, a lower temperature gives higher loading which can be seen in the figure since $b \propto \exp(1/T)$ (a lower temperature gives a higher b).

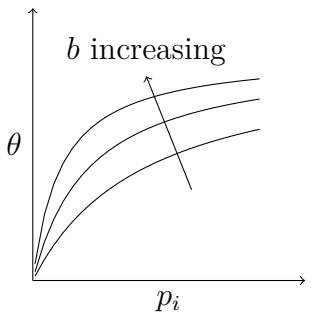

Figure 2.5: The characteristics of the Langmuir isotherm.

2.3.2 Polanyi's potential theory of adsorption and the Dubinin-Astakhov isotherm

While the Langmuir isotherm is simple, it might not be sufficient in order to capture the characteristics of more complex adsorption system. A different approach was used by Polanyi who assumed that there exist an adsorption potential, denoted ε.

Polanyi's adsorption potential is a function of the distance between the adsorbent surface and a molecule. The potential can be defined as

$$\varepsilon = f(W) \tag{2.8}$$

where W is the weight adsorbed (which is interchangeable with the height of the adsorption layer if its density is assumed constant), and f is some kind of distribution function. (Bansal & Goyal, 2005, p.113)

Figure 2.6 shows the equipotential surfaces as a function of distance from the adsorbent surface. The equipotential surfaces have the same closest distance to the surface thus the same adsorption potential. Figure 2.7 shows the characteristic curve where the characteristics of adsorption potential is shown. If the distance to the adsorbent surface is very small, the adsorption potential become very high while a large distance implies a low adsorption potential. When the distance is large enough, there is no potential for adsorption.

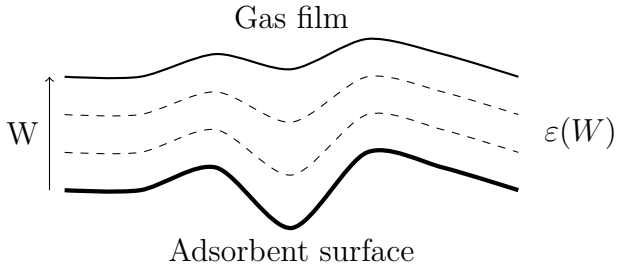

Figure 2.6: Equipotential surfaces $\varepsilon(W)$ between the gas film and the adsorbent

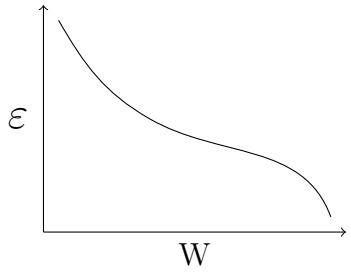

Figure 2.7: The characteristic curve for an arbitrary adsorbate-adsorbent system

If the temperature of the system is well below the critical temperature for the adsorbate, the state of the adsorbate can be considered liquid. If the liquid is also considered incompressible, the potential for adsorption could be written in terms of saturation vapor pressure:

$$\varepsilon = RT \ln(p_i^*/p_i) \tag{2.9}$$

where R is the universal gas constant, T is the temperature, p_i is the partial pressure for species i, and p_i^* is the saturation vapor pressure. (Bansal & Goyal, 2005, p 114)

2.3.2.1 The Dubinin-Astakhov isotherm equation

Dubinin and coworkers expanded Polanyi's potential theory of adsorption. If the adsorption potential can be written as a function $\varepsilon = f(W)$ it can be assumed that an inverse relation is also possible, writing the equilibrium loading as an inverse function of the adsorption potential: $W = f^{-1}(\varepsilon)$. Dubinin used a Weibull distribution with the adsorption potential, raised to a adsorbent-dependent power, as the variable. While the equation can look fairly empirical, authors like Chen and Yang (1994) have derived the equation from statistical mechanics.

Using the adsorption potential, the Dubinin-Astakhov equation can be written as

$$W = W_0 \exp\left[-K\left(\frac{\varepsilon}{\beta}\right)^n\right] \tag{2.10}$$

where W is the adsorbed weight, W_0 is the maximum adsorbed weight, K is a constant characterizing the pore-size distribution of the adsorbent, β is the affinity coefficient which correlates different vapors in the adsorbate-adsorbent system[2], and n is the Dubinin-Astakhov power coefficient. (Do, 1998, p.159)

Using eq. (2.9) in eq. (2.10) and rewriting the exponent constants to a characteristic energy $E = \beta/K^{1/n}$ gives

$$W = W_0 \exp\left[-\left(\frac{RT\ln(p_i^*/p_i)}{E}\right)^n\right] \tag{2.11}$$

Equation (2.11) is visualized in fig. 2.8 where the adsorption potential is fixed and the free variables are varied.

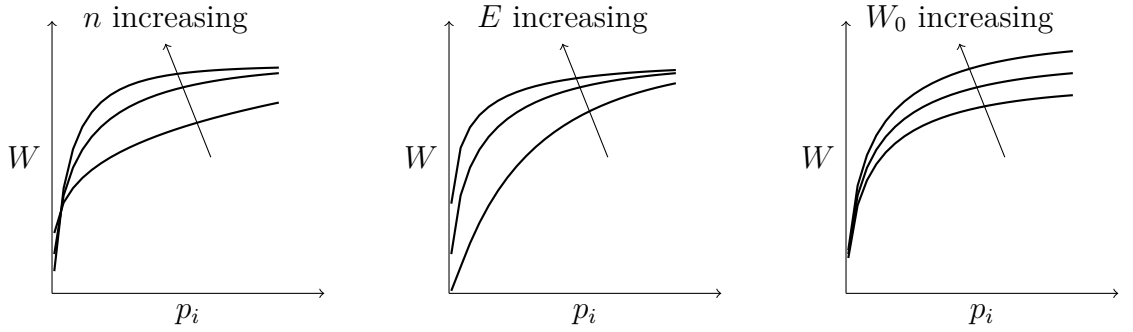

(a) Varying the power coefficient n

(b) Varying the characteristic energy E.

(c) Varying the maximum absorbed amount W_0.

Figure 2.8: The Dubinin-Astakhov isotherm characteristics with a fixed adsorption potential

[2]Benzene is usually used as a standard adsorbate with $\beta = 1$

2.3.2.2 Tuning the Dubinin-Astakhov isotherm

For the Dubinin-Astakhov isotherm, eq. (2.11), three parameters (W_0, n and E) need to be found. The equilibrium partial pressure in the adsorption potential, eq. (2.9), can be described as the vapor pressure, expressed as a temperature dependent Antonie equation. There is also a possibility to have a temperature correction factor and in this case Dubinin (1975, p.12) modifies eq. (2.11) so that the equation includes a correction in the exponent. The isotherm is corrected for a temperature deviation from the temperature T_0:

$$W = W_0 \exp\left[-\left(\frac{RT\ln(p_i^*/p_i)}{E}\right)^n - \alpha(T - T_0)\right] \tag{2.12}$$

where α is thermal coefficient of limiting adsorption.

Jakubov and Mainwaring (2002) have further corrected the Dubinin-Astakhov isotherm in order to better account for thermodynamic incorrect behaviour.

2.3.3 Kinetics and the linear driving force

Isotherms lack information about how fast a reaction is happening. Consider the reaction $\mathrm{S} + \mathrm{X} \rightleftharpoons \mathrm{SX}$ where the molecule X is adsorbing onto a vacant site S forming the adsorbed state SX. The double arrows denote that the reverse reaction could also take place, when a molecule is desorbing from the site resulting in a vacant site and a free molecule.

The reaction could be expressed in two ways, either as two counteracting reactions or as one reversible reaction. Having two counteracting reactions means one reaction for adsorption and one reaction for desorption both with a non-negative sign, like eq. (2.4) and eq. (2.5) for the Langmuir isotherm.

A kinetic expression could also be formed for the reaction $\mathrm{S} + \mathrm{X} \overset{r}{\longleftrightarrow} \mathrm{SX}$ with only one reaction rate. This is done by having a driving force between the current state and an equilibrium state. The easiest expression is the linear driving force model (LDF) which is written like

$$r = k(\theta_{eq} - \theta) \tag{2.13}$$

where r is the total reaction rate, k is a time constant, θ_{eq} is the equilibrium loading and θ is the fractional local coverage.

Equation (2.13) could be either positive or negative for a reaction, where a positive sign implies adsorption and a negative sign implies desorption. While reaction rates were available already when deriving the Langmuir isotherm in section 2.3.1, the Dubinin-Astakhov isotherm does not include any information about the reaction rates. The LDF model is powerful since the Dubinin-Astakhov isotherm equation, or any other isotherm equation, could easily be put into a reaction rate expression.

Do (1997) discusses the linear driving force among other driving force models.

2.4 Breakthrough and bleed emissions

As previously stated, the carbon canister has a limited capacity and therefore the canister must be sized accordingly to the regulations present.

2.4.1 Breakthrough

When the canister is loaded (see fig. 2.2a) it will eventually run out of vacant sites on which the hydrocarbons can adsorb. This means that hydrocarbon concentration out in the atmosphere will be non-zero and a *breakthrough* occurs. The breakthrough can be expressed either as a cumulative mass or as an instantaneous concentration.

If the canister were ideal, isothermal, and functioned as an ideal plug flow reactor (PFR), the breakthrough would look like a unit step function with the same concentration in and out of the canister. A real canister is non-isothermal, has granulated pellets and the geometry and inlet conditions are not ideal, hence the breakthrough characteristics can heavily differ from an ideal PFR.

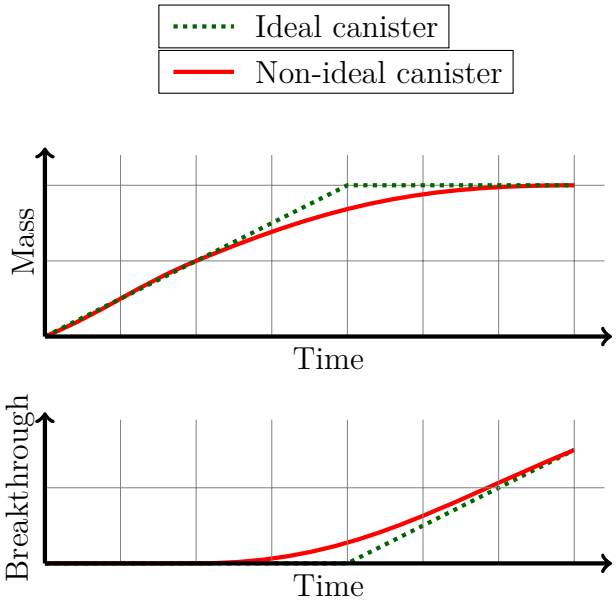

Figure 2.9: The canister mass and cumulative breakthrough for an ideal and a non-ideal canister

In fig. 2.9 the characteristics for an ideal and a non-ideal canister can be seen. The canisters are both loaded with a constant rate of an adsorbate. While both canisters have the same maximum capacity, an earlier cumulative breakthrough mass is observed for the non-ideal canister.

The breakthrough itself is important since this generally is how regulations are tested, but the breakthrough characteristics are also important since it can be used as a measurement of how ideally the canister behaves, without further looking into the detailed design of the canister. This measurement is described by Knaebel (2008, pp 1141-1144) where the non-ideal breakthrough is caused by dispersion and diffusion.

2.4.2 Diffusion and bleed emissions

Even if there is no convective flow going through the carbon bed, diffusion will take place in the gaseous phase due to a concentration gradient. The diffusion phenomenon is important for long term events where breakthrough will happen not due to capacity limitations or non-isothermal effects, but rather because of diffusion. This breakthrough event is called bleed emissions and these emissions are in the orders of tens or hundreds milligrams per day.

The diffusive bleed emissions can be controlled by having a *longer* carbon bed, a high purging flow, or airbeds in between the carbon bed as reported by Itakura, Kato, Kohama, Hyoudou, and Murai (2000). The use of an auxiliary chamber, filled with a long monolith carbon bed, is popular today since it will have a low pressure drop and can reduce bleed emissions efficiently, as reported by Williams and Clontz (2001).

2.5 CFD calculations and 1D-models

Computational fluid dynamics (CFD) is a powerful tool for simulating flow fields within different geometries, reducing cost and time in engineering applications. CFD applications iteratively solve the desired transport equations, together with the continuity equation and a pressure equation for a case described by boundary conditions, initial conditions, and a computational mesh.

One dimensional (1D) models can be seen as the simplest case in CFD modelling. The one and only dimension can be efficiently used in applications such as pipes and valves with pressure drops, where the radial and tangential components can be neglected. The discretization of a plug flow reactor in 1D can be seen in fig. 2.10 where the properties are first described by axial position but in the discritized case become lumped together for each computational cell.

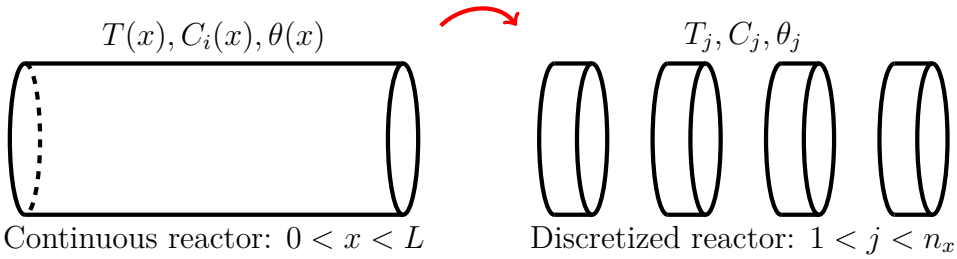

Figure 2.10: Discretization of a plug flow reactor

For this thesis, the carbon canister is going to be described in 1D. Properties like velocity, pressure, temperature, reactions and concentrations are all possible to simulate using a 1D CFD approach.

2.5.1 Equations solved in GT-Suite

GT-Suite solves a number of equations in order to be able to describe the different properties. The quantities which are described as a vector, like velocity and mass fraction fluxes, are calculated at the boundaries at each computational cell while scalar quantities like temperature and pressure are calculated at the centroid of the cells.

Firstly there is the continuity equation, the energy equation and the momentum equation which are all solved together for the flow, calculating velocities and pressures along the computational grid. (Gamma Technologies, 2015)

The continuity equation:

$$\frac{dm}{dt} = \sum_{\text{boundaries}} \dot{m} \tag{2.14}$$

where m is the mass, t is the time, and $\dot{m}$ is the mass flow.

The enthalpy equation:

$$\frac{d(\rho HV)}{dt} = \sum_{\text{boundaries}} (\dot{m}H) + V\frac{dp}{dt} - hA_s(T_{\text{fluid}} - T_{\text{wall}}) \tag{2.15}$$

where ρ is the density of the fluid, H is the total enthalpy, V is the volume, p is the pressure, h is the heat transfer coefficient, A_s is the heat transfer surface area, and T is temperature.

The momentum equation:

$$\frac{dm}{dt} = \frac{dpA + \sum_{\text{boundaries}}(\dot{m}u) - 4C_f\frac{\rho u|u|}{2}\frac{dxA}{D} - C_p(\frac{1}{2}\rho u|u|)A}{dx} \tag{2.16}$$

where A is the cross sectional flow area, u is the velocity, C_f is the skin friction coefficient, dx is the discritization length, D is the equivalent diameter, and C_p is the pressure loss coefficient.

GT-Suite also solves a number of equations for the chemical reactions. These equations are solved using another type of solver which for each time step provide the solution of the chemical reactions. The equations are the soild phase energy equation, the gas phase energy equation, the continuity equation, the momentum equation as well as other equations presented below. (Gamma Technologies, 2015)

Solid phase energy equation:

$$\psi_s\frac{\partial T_s}{\partial t} = \frac{\partial}{\partial z}\left(f_{sb}\lambda_{sb}\frac{\partial T_s}{\partial z}\right) + hS(T_g - T_s) - \sum_{j=1}^{nrct} a_j\Delta H_j r_j + \frac{P}{V} + h_x S_x(T_x - T_s) \tag{2.17}$$

where ψ_s is the efficient volumetric heat capacity, T_s is the temperature of the gas at the surface, z is the axial position, f_{sb} is solid fraction of substrate, λ_{sb} is the thermal conductivity of the substrate, h is the heat transfer coefficient, S is the surface area per reaction space volume, T_g is the temperature of the bulk gas, a_j is the active site density of reaction j, ΔH_j is the enthalpy of reaction of reaction j, r_j is the reaction rate for reaction j, P is the power input, V is the reaction volume, h_x is the external heat transfer coefficient, S_x is the external surface area per reaction volume, and T_x is the external temperature.

Gas phase energy equation:

$$\varepsilon \rho_g v C_{pg} \frac{\partial T_g}{\partial z} = hS(T_s - T_g) \tag{2.18}$$

where ε is the void fraction of the reaction space, ρ_g is the density of the bulk gas, v is the interstitial velocity, and C_{pg} is the heat capacity of the gas.

Continuity equation:

$$\frac{\partial}{\partial z}(\rho_g v) = 0 \tag{2.19}$$

Momentum equation:

$$\varepsilon \frac{\partial p}{\partial z} + \varepsilon \rho_g v \frac{\partial v}{\partial z} = -Sf \frac{1}{2} \rho_g v^2 \tag{2.20}$$

where p is the pressure and f is the friction factor.

Coverage continuity:

$$\sum_k \theta_k = 1 \tag{2.21}$$

where θ_k is the surface coverage component for coverage k

Coverage reactions:

$$\frac{d\theta_k}{dt} = \sum_j \sigma_{kj} r_j \tag{2.22}$$

where σ_{kj} is stochiometric coefficient for coverage k in reaction j.

Mass fraction transport equation:

$$\varepsilon \rho_g v \frac{\partial \omega_g}{\partial z} = k_{m,i} S(\omega_{s,i} - \omega_{g,i}) = \sum_j s_{ij} a_j r_j \tag{2.23}$$

where ω_g is the mass fraction in the bulk gas, $k_{m,i}$ is the mass transfer coefficient for species i, and $\omega_{s,i}$ is the mass fraction in the washcoat for species i.

It should be noted that some equations assumes a short residence time for the chemical reactions compared to other scale of modelling. This implies a quasi-steady approximation where the substantial derivative is replaced with a simpler spatial derivative. (Gamma Technologies, 2015)

2.6 Literature review

Different types of studies have been carried out, where some papers focus more on modelling and simulation, while others have a larger perspective of the canister. There are also studies done only on the activated carbon but the methods of this thesis are assumed to work well with respect to all kinds of carbons, hence no detailed literature review has been done on different types of activated carbon.

2.6.1 Modelling and simulation of hydrocarbon adsorption on activated carbon

Previous work has been done in modelling the adsorption and desorption, the earliest by Lavoie, Johnson, and Hood (1996) who used experimental results to predict the 1D transient behaviour of a carbon canister. The resulting model predicts the behaviour well and it is therefore assumed to be possible to capture the same kind of phenomena in this project.

Fiani, Perier-Cambry, and Thomas (2000) proposed a kinetic model using both mass and heat transfer which describes experiments well. The experimental set up used a small solid carbon sample (30 mg) which is good since the thermal conditions could be controlled and measured in detail. The paper does not handle canister purging. The paper provides a good discussion about convective and conductive heat transfer around and within the carbon sample. The paper can be seen as a follow up to the article by Fiani, Perier-Camby, Thomas, and Sanalan (1999), which is written by the same authors.

Bai et al. (2004) use a 2-dimensional CFD model to simulate the adsorption and desorption over a carbon bed. In this study, results and parameters found in the literature and other studies are only used, hence no strong validation of the accuracy could be carried out.

Sato, Kobayashi, and Hasatani (2009) made a 3-dimensional CFD model which even with a low resolution ran as slow as half of real time. Because of this, the model was simplified by using a linear driving force model which ran about 100 times faster which was still sufficient enough to predict results accurately. The same authors later wrote a paper (Sato & Kobayashi, 2011) which describes another 3D CFD model which also was used to simulate diurnal diffusion effects. This paper also investigated numerical aspects like the effect of the time step used.

Lin, Dong, Ali, Hipp, and Schnepper (2012) used a Dubinin-Astakhov isotherm model for canister performance in a CFD model. An interesting approach for predicting the adsorbed fuel vapor is used by having a ”Lagrange Interpolating Polynomial” where a quadratic dependency from fuel vapor concentration and temperature is used. The paper however does not reveal any data or parameter values which have been obtained.

Smith et al. (2015) used a simple approach where a 1D model canister model is calibrated using the enthalpy of formation and ratio of adsorption/desorption rate for a Langmuir model. The model is then expanded to better simulate a real world purge valve.

2.6.2 Canister design studies

The articles presented here might not model and simulate the carbon bed within the canister but rather look at larger quantitative parameters like measured breakthrough.

Mellios and Samaras (2007) used an empirical model for describing the loading and purging of the canister. The authors do not model the canister itself but rather the breakthrough and the paper lacks detailed chemical and thermal modelling which

is of interest in this thesis.

Williams and Clontz (2001) focus on bleed emissions from canisters and how to efficiently design a canister for minimal bleed performance. No modelling is done and straight data is presented with conclusions on how to minimize these diffusion based effects.

Reddy (2012) looks at the vapor generation from the fuel tank along with required canister size in order to trap the evaporated fuel. Bleed emissions are also of interest in the report where a correlation between bleed emissions and purged air volume is created.

Zaremba and Jennings (2011) quantify the canister performance under a driving cycle. The paper uses an approach where the fuel fraction out of the canister during purge is described as a function of cumulative purge flow.

Itakura et al. (2000) looks at bleed emissions and diffusion in canisters. The authors look at how an airbed between a loaded and an unloaded canister affects the diffusion and the knowledge is used to design a new canister which reduced the diurnal breathing loss by 50%.

Yamasaki et al. (2009) calculates the diffusion rate of n-butane in a carbon bed and finds a value for this parameter. The same approach is used to calculate the diffusion rate at different temperatures in the paper by Kuronuma, Masuda, Kobayashi, Sato, and Yamasaki (2011), however with limited success.

2.6.3 What is different in this thesis?

As presented in section 2.6.1 multiple authors have done simulations before, however the field is far from well researched. This thesis compares the Langmuir adsorption model and the Dubinin-Astakhov isotherm LDF model for a 1D canister. While Lin et al. (2012) uses a interpolation method for the DA-isotherm, a universal isotherm equation is found in this thesis. Generally the articles and papers cited above models loading only until a small breakthrough occurs while this thesis includes experiments and simulation past the breakthrough, which is important in order to capture non-isothermal effects. This thesis also investigate radial heat transfer and canister orientation. The thesis also presents a complete set of parameters used in order for a reader to replicate the simulation results.

3

Experimental methods

This chapter describes the experiment setup, and the experiments and tests carried out in order to gain the results presented later.

3.1 Experimental setup and canister geometry

In order to have experimental data which is as good as possible, an experimental canister was built. This canister was prepared with multiple thermocouples in order to be able to measure temperature throughout the canister.

3.1.1 Canister geometry

Two experimental canisters were constructed. A sketch of a canister can be seen in fig. 3.1. One litre of Ingevity BAX-1500 activated carbon was put in the middle of a plastic pipe. The carbon was held in place by a plastic foam placed in between the carbon and a perforated metal panel. The metal panel was fixed by screws going through the plastic pipe. The top and bottom of the plastic pipe was sealed with a translucent acrylic glass. Connections were put in place at the very top of the plastic housing, and in the lower side so that the canister can easily be put on a balance.

The reason for constructing two identical canisters was so that the experiments could be verified independently of which canister was used.

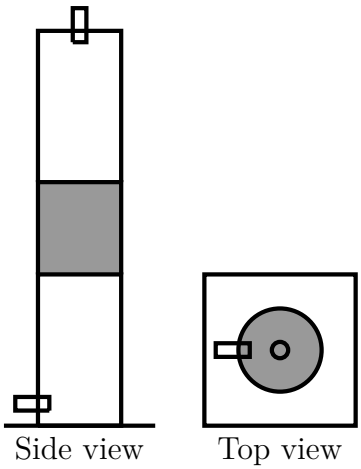

Figure 3.1: Geometry of the experimental canisters

3.1.2 Pressure drop connections and thermocouples

Firstly the canisters were prepared with four holes in order to be able to measure the pressure drop over the two filters as well as over the carbon bed. After the holes were drilled, four small copper pipes (30 mm long and with a diameter of approximately 5 mm) were put inside the holes and glue was applied around the pipes in order to make sure leakage was avoided.

In order to measure the temperature of the canisters, the canisters were prepared with thermocouples. One of the canister was prepared with 20 thermocouples and the other one was prepared with 8 thermocouples put in positions so the results of the first canister could be validated with the second canister.

The thermocouples were labeled 1 through 28 and their positions for the canister with most thermocouples can be seen in fig. 3.2 where the red cylinder represent the carbon bed. Note that two sensors are missing from the total of 20 sensors in fig. 3.2, these sensors are placed over and under the carbon bed in order to measure the temperature of the incoming flow and the outgoing flow. A table of the complete temperature sensor positions for both canisters can be found in appendix B.

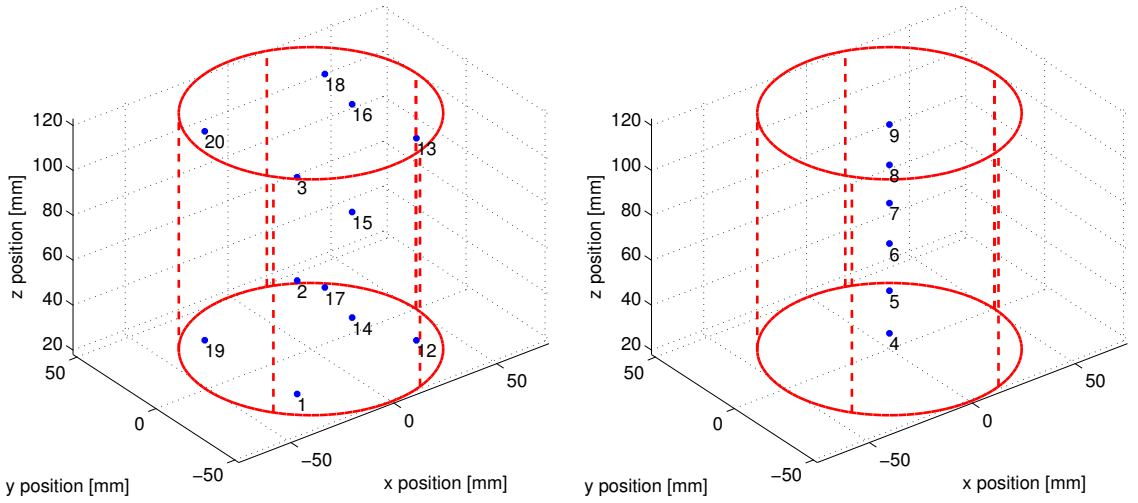

(a) Temperature sensors in Canister 1 (b) Additional sensors in Canister 1

Figure 3.2: The temperature sensor positions for canister 1.

3.1.3 Experimental setup

One experimental canister, as described in section 3.1.1, was put onto a Sartorius LP5200P balance. The balance was connected to a computer were the output of the balance was recorded continuously. The thermocouples were connected to a Ipetronik M-Thermo K16 measuring module which also made it possible to record the temperatures continuously. A Matlab script was written in order to combine and visualize the data from the balance and the thermocouples.

In the loading experiments, the inlet was connected to a flow regulator which controlled the flow of a n-butane/nitrogen mix using manually controlled rotameters.

The mixture of n-butane and nitrogen is commonly used for testing in order to eliminate errors from using different types of gasoline with different compositions.

A ventilation hose was put over the outlet, making sure that no butane breakthrough leaked out into the ambient air. An overview of the experimental setup for the loading experiments can be seen in fig. 3.3.

During the purging experiments, the inlet was connected to a vacuum pump which created a backflow through the canister, much like a real canister function. The flow could be manually controlled and the flow was here also indicated by a rotameter. Note that with this approach purging is carried out with air and not pure nitrogen since the second connection was not connected to anything but the ambient air. The setup is almost identical to the loading event as seen in fig. 3.3, but with the mass flow regulator connected to a vacuum pump instead of gas bottles.

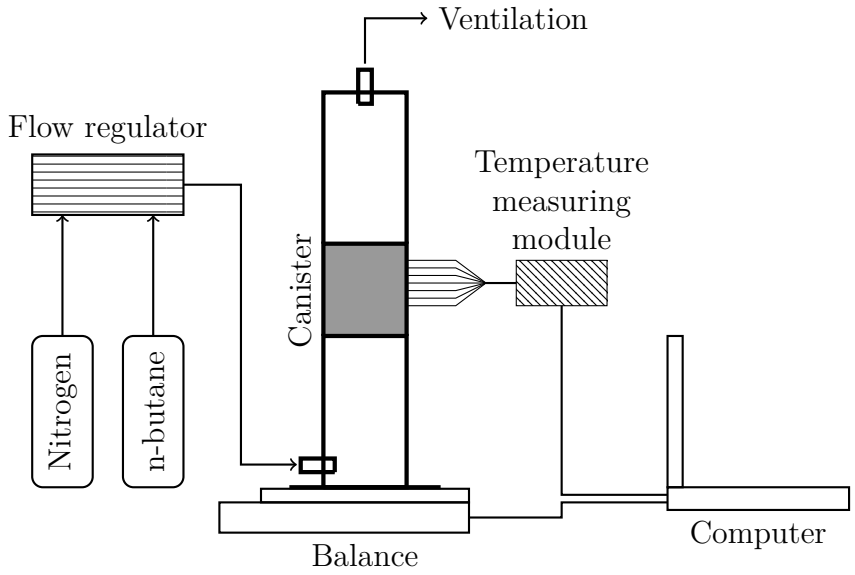

Figure 3.3: Exprimental setup during loading events

3.2 Experiments and tests

The number of tests and the conditions such as flow rates and concentrations must be considered carefully in order to obtain an appropriate trade off between time for experiments and the accuracy of the model that was going to be developed.

3.2.1 Pressure drop

In order to measure the pressure drop over the carbon bed the canisters were connected to a test rig where the incoming air flow was varied between 0 and 100 litres per minute. The pressure drop was measured with multiple pressure gauges in the four different positions described in section 3.1.2. A picture of the setup is shown in fig. 3.4. Note that the canister in the picture has not yet been prepared with thermocouples.

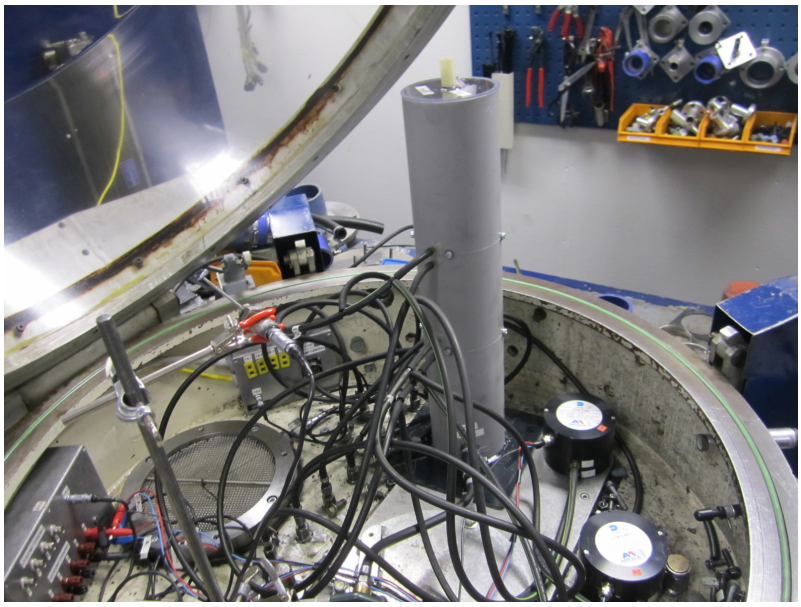

Figure 3.4: Experimental setup of the pressure drop measurements

3.2.2 Loading

As described in section 2.1.1, the flow rates for slow and fast loading are very different and since those events can be hard to measure, a flow rate of something in between in considered. The experimental setup allows for butane flow rates of 20 grams per hour up to 200 grams per hour. The concentrations of air/butane in a real fuel tank vary depending on temperature and fuel type as investigated by Reddy (2012) who reports volumetric fuel concentrations in the order of 30% to 50%.

Three different loading rates were tested along with two different concentrations. The loading rates were 36.5, 70 and 100 grams of n-butane per hour. The volumetric concentrations were 35% and 45%. The loading experiments were labeled case A through F as described in table 3.1. The canister was purged for at least three hours at a flow rate of 20 litres of air per minute in order to make sure the canister had the same initial condition for each experiment.

	Concentrations	
Butane flows	35 %	45%
36.5 g/h	Loading A	Loading B
70 g/h	Loading C	Loading D
100 g/h	Loading E	Loading F

Table 3.1: Loading experiments

While the experimental setup allowed for even higher butane flow rates, the resulting concentration would be higher than 50% and hence 100g/h was the upper limit. The lower limit could be lower than 36.5g/h but it would increase the time for experiments as well as lowering the accuracy since the rotameters does not have a perfect accuracy.

3.2.3 Purging

The purging experiments were carried out starting with a canister which had been saturated with a 45% volumetric concentration of n-butane. For the purging events, the experimental setup allowed constant air flow rates of 5 litres per minute to 30 litres per minute. Three different flow rates were investigated: 9.14, 17.72 and 25.20 litres of air per minute (LPM) labeled A, B and C as presented in table 3.2. The flow rates were selected because they corresponded to a simple value read on the rotameter.

Air flow rate	Case label
9.14 LPM	Purge A
17.72 LPM	Purge B
25.20 LPM	Purge C

Table 3.2: Purging experiments

3.2.4 Canister orientation

In order to investigate if the canister orientation influences the adsorption characteristics, the canister was also orientated in a horizontal position instead of a vertical orientation. Figure 3.5 shows how the vertical orientation and the horizontal orientation have different gravity vectors.

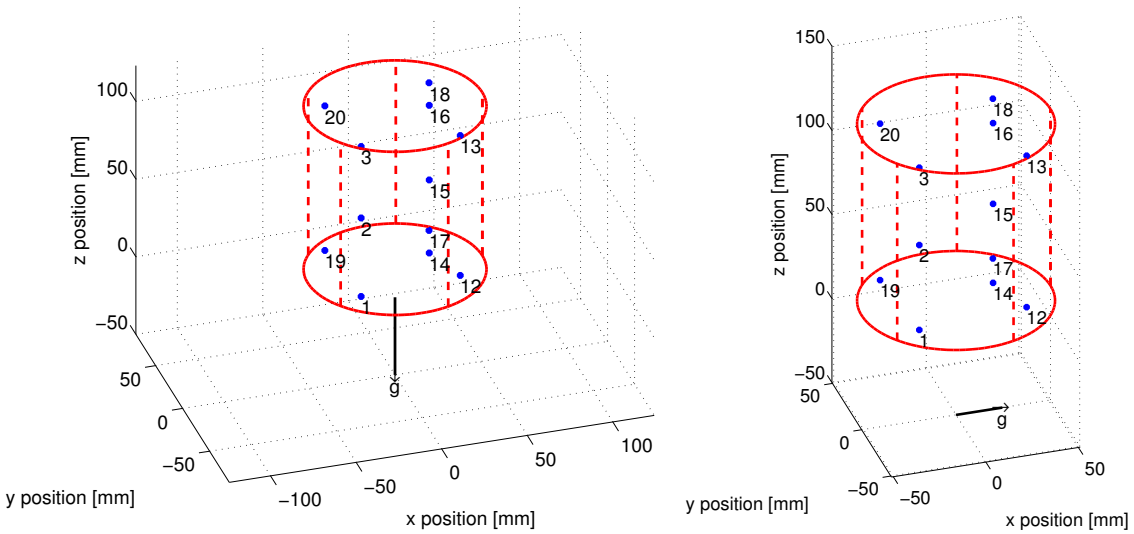

(a) Vertical orientation

(b) Horizontal orientation

Figure 3.5: The different orientations of the canister, with gravity vectors plotted

4
Simulation methods

The CAE application GT-Suite is used for simulations. The application can simulate the chemical reactions as well as compare simulations and experiments in order to fine tune parameters.

4.1 Solver settings

In GT-Suite a continuous Time Control Flag was set in order to make the simulation a transient one. An implicit solver flow field solver was used with a time step varying dependent on the simulation case. The ability to vary the time step can drastically improve simulation time. A larger time step can be used where slower dynamics are observed for example in the later phase of a purging event.

A Backward Differential Formulations (BFD) solver were used for solving the chemical reaction equations. Other settings were left as their default values in GT-Suite.

Multiple parameters are defined as *case parameters* which means the parameters can easily be varied and set up as multiple cases. Different cases are easy to compare and post process in GT-Suite.

4.2 Objects and project map

The simulations carried out in GT-Suite modeled the canister as a subassembly model with two connections to the outside of the subassembly. This means that different files could be created which all were connected to the same subassembly model. Three different files were used in this thesis, one for the pressure drop calibration, one for all the loading events and one for all the purging events. These files simply include different boundary conditions. For example the loading event and the purging event have different boundary conditions since the flow is reversed in the purging case. The three files include the very same canister subassembly, in which the internals of the canister is modeled.

The canister subassembly is shown in fig. 4.1. The main component is the `CatalystBrick` object labeled CarbonBed which a chemical reaction object is connected to, in this case the `Fixed-Dubinin-Astakhov` surface reaction object. The lower part of fig. 4.1 includes monitors and calculations in order to monitor and optimize the model. Interested readers are refereed to GT-Suite's manuals for further information about components not covered here.

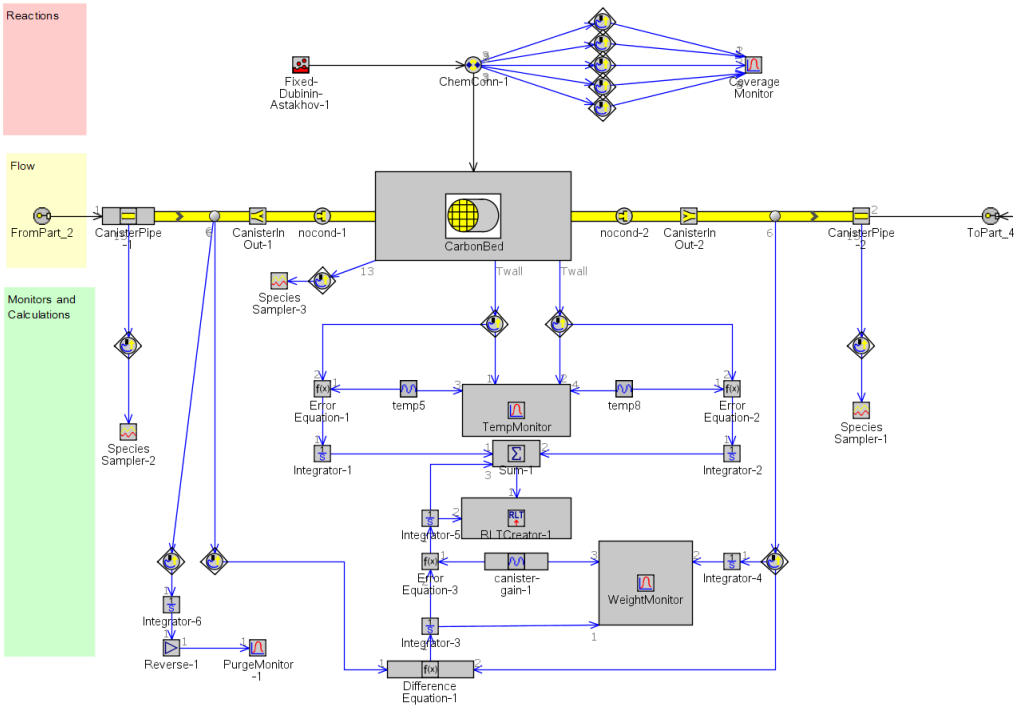

Figure 4.1: The canister subassembly in GT-Suite.

4.2.1 The `CatalystBrick` object

The `CatalystBrick` object was used to model the carbon bed and has a number of settings. The `CatalystBrick` object is a monolith with a substrate material so that the flow is assumed to flow within the channels of a monolith.

The Channel Geometry was set to square and the cell density was set to $1\,\mathrm{mm}^{-2}$. The Channel Geometry and the cell density were assumed to be parameters that could be fixed to that only the substrate wall thickness could be varied in order to match the pressure drop, as described in section 5.2.1.

The geometry such as the frontal area, length, and discretization length were set as case parameters so that it could easily be varied, but their values for the non-sensitivity analysis simulations are shown in table 4.1.

Property	**Value**
Frontal area	$8172\,\mathrm{mm}^2$
Length	122 mm
Discretization Length	5 mm

Table 4.1: The geometry properties for the `CatalystBrick` object

A ”Detailed Wall Layer Geometry and Temperature Solver”-object was specified. The wall thickness was set as a case parameter so that it could be optimized in order to match the pressure drop over the carbon bed. The material of the carbon bed was specified, and the plastic housing of the canister were defined as a 3 mm thick material. The external temperature as well as the external heat transfer coefficient was defined. The properties of this object are defined in table 4.2. While some

of this data is estimated and provided here without references, the properties are also a matter of optimization. It should be noted that the carbon bed density is much higher than the apparent density of real activated carbon in order to take into account the adsorbed adsorbate which changes the properties of the carbon bed.

Property	**Value**
Carbon bed thermal conductivity	$0.1\,\mathrm{W/(mK)}$
Carbon bed density	$560\,\mathrm{kg/m^3}$
Carbon bed specific heat	$1000\,\mathrm{J/(kgK)}$
External Convection Coefficient	$10\,\mathrm{W/(m^2K)}$
Plastic housing thermal conductivity	$1\,\mathrm{W/(mK)}$
Plastic housing density	$900\,\mathrm{kg/(m^3)}$
Plastic housing specific heat	$1800\,\mathrm{J/(kgK)}$

Table 4.2: The Detailed Wall Layer Geometry and Temperature Solver object used for the `CatalystBrick` object

4.2.2 The `SurfaceReactions` object

A `SurfaceReactions` object is connected to the `CatalystBrick` object. This object is used to specify the chemical reactions which happen on the surface of the `CatalystBrick` .

The species n-butane and nitrogen was defined as species that should be reacting and solved for. The turnover number was selected as the Rate Expression Basis, which means that rate expressions are entered with units of moles per second per moles of active sites. The Concentration Specification was selected to moles per square metre and the transient Diffusion option was selected in order to have a gradient between surface concentration and bulk concentration.

The active site density was selected to be a case parameter so that it could be varied easily. Two coverages were created, one represented a vacant site S, with one site element atom, and the other coverage represented an occupied site SX, with one site element atom, four carbon atoms, and ten hydrogen atoms. The enthalpy of formation for the occupied site was also selected to be a case parameter.

The reaction rate for the `SurfaceReactions` object is defined as

$$r = A \times T^b \exp(-E_A/RT) \times f(\{conc_j\}, G(i)) \times f(A(j)) \tag{4.1}$$

where A is a pre-exponential factor, T is the temperature, b is a temperature exponent, E_A is the activation energy, R is the universal gas constant, f is an arbitrary function, $\{conc_j\}$ is the concentration of species j, $G(i)$ is a general/inhibitor function which can include pressure, temperature, concentration as well as mathematical expressions, and $A(j)$ is the coverage of species j.

4.2.2.1 The Langmuir reaction

In order to model the Langmuir reaction, two reactions were defined. The first reaction is the adsorption reaction $\mathrm{S} + \mathrm{X} \longrightarrow \mathrm{SX}$ where X represents the n-butane molecule.

For the adsorption reaction, the variables in eq. (4.1) are defined. The pre-exponential factor was set to a case parameter, the temperature exponent and the activation energy was set to 0, the $f(\{conc_j\}, G(i))$-function was set to $\{conc_{n-butane}\}$ and the coverage expression was set to $A(S)$ representing the fraction of vacant sites.

For the desorption reaction, SX $\longrightarrow$ S + X, the pre-exponential factor and the activation energy were set to be case parameters, the temperature exponent was again set to 0, the $f(\{conc_j\}, G(i))$-function was set to 1 and the coverage expression was set to $A(SX)$ representing the fraction of occupied sites.

The reactions is now defined as described in section 2.3.1:

$$\mathrm{S} + \mathrm{X} \underset{r_{des}}{\overset{r_{ads}}{\rightleftharpoons}} \mathrm{SX} \tag{4.2}$$

$$r_{ads} = k_{ads}\{conc_{n-butane}\}(1-\theta) \tag{4.3}$$

$$r_{des} = k_{des}\exp(-E_A/(RT))\theta \tag{4.4}$$

4.2.2.2 The Dubinin-Astakhov LDF model

The Dubinin-Astakhov isotherm was modeled with the LDF model which were described in section 2.3.2 and section 2.3.3.

Only one reaction was defined. In eq. (4.1) the pre-exponential multiplier was set as a case parameter, the temperature exponent and the activation energy was set to 0, the coverage expression was set to 1, and the $f(\{conc_j\}, G(i))$-function was set to $G(1) - A(SX)$.

The function $G(1)$ was defined as the equilibrium fraction of occupied sites in the Dubinin-Astakhov isotherm as eq. (2.11) but divided by W_0 which is accounted for by the active site density. The Antonie equation was used to describe the saturation water pressure and the Antonie equation parameters for n-butane are taken from Lange and Dean (1973). A "max" function limits the n-butane concentration in order to control that division by zero does not happen. $G(1)$ is explicitly defined as:

$$G(1) = \exp\left[-\left(\frac{8.3145 \times T \times \ln\left(\frac{133.3\times 10^{6.83029-\frac{945.9}{240+T}}}{\frac{max(\{conc_{n-butane}\},1e-8)}{(101325/(8.3145\times T))}}\right)}{[DA\_E]}\right)^{[DA\_n]}\right] \tag{4.5}$$

where $[DA\_E]$ and $[DA\_n]$ are case parameters.

This defines the Dubinin-Astakhov isotherm with a linear driving force which is controlled by the pre-exponential multiplier (LDF time constant) k:

$$r = k(G(1) - \theta) \tag{4.6}$$

4.3 Initial conditions and boundary conditions

The initial conditions for all parts were set to the temperature of 23 °C and a pressure of one atmosphere. The boundary conditions were in the loading case set to an `EndFlowInlet` object for the inlet and an `EndEnviroment` object for the outlet. For the purging case the flow was reversed but the same type of components were used.

4.4 Loading and purging simulations

The simulations were set up in order to replicate the conditions in the experimental setup. The inlet conditions for the loading experiment can be seen in table 4.3 where the composition is the volumetric fraction. The time step for the loading simulations was set to 0.05 s for the first 500 seconds of the simulation, and then linearly increased to 0.8 s at 6000 seconds.

Loading case	**Total flow rate** (g/h)	**Max simulation time**	**Composition**
A	68.65	12000 s	35%
B	57.45	17000 s	45%
C	133.58	10000 s	35%
D	112.69	10000 s	45%
E	189.48	10000 s	35%
F	158.51	8000 s	45%

Table 4.3: Simulations of loading experiments

For the purging experiments, the inlet conditions can be seen in table 4.4 and it should be noted that nitrogen is set as the incoming species at 100% concentration. The time step for the purging experiments was set to 0.02 s for the first 500 seconds and then increased linearly to 0.8 s at 5000 seconds.

Purge Case	**Total flow rate** (g/h)	**Max simulation time**
A	675	6000 s
B	1308	6000 s
C	1860	6000 s

Table 4.4: Simulations of purging experiments

4.5 Sensitivity analysis simulations

With a good mathematical model, it will be possible to simulate changes to the canister in order to maximize the performance. In this thesis four different changes was considered. The changes will either change the geometry of the canister or change the thermal properties, in order to gain performance.

4.5.1 Benefits, cost of change and response variables

In order to measure how well a certain change performs, there must be some kind of cost and benefit. There might however be no simple way to quantify how much a car benefits from a certain change and there might also be no simple way to quantify the cost. The benefits could be a cheaper canister, a decreased purge flow or a decreased pressure drop over the canister, just to take a few examples. The costs

can be a bigger canister, an earlier breakthrough time, increased purge flow, or the introduction of a new component/material within or around the canister.

Because of these problems, this thesis does not rank which change will be best in terms of performance since both the cost and benefit are hard to quantify.

4.5.2 Parameters to be varied

Four different changes will be considered. The parameter(s) as well as the idea is described for each change below.

Length/diameter ratio. Decreasing this ratio will likely reduce the pressure drop and possibly make the desorption go faster by decreasing the length of the adsorption front. The specification of this sensitivity analysis can be seen in table 4.5.

Case	**Frontal Area** (mm^2)	**Length** (mm)	**L/D**
L/D low	12258	81.58	1.3
L/D mid	8172	122	2.4
L/D high	5448	183.5	4.4

Table 4.5: Sensitivity analysis of the length/diameter ratio

Temperature of the incoming purge flow. A high temperature helps the desorption, and thus an increased temperature will likely make the carbon bed release the hydrocarbons faster in the purging case.

The temperatures simulated will be 45 °C and 70 °C as well as the base case of 23 °C .

External heat transfer coefficient and external temperature. In order to minimize the thermal effects, increasing these parameters would likely make the canister more isothermal and ideal in its performance, both for purging and loading.

A loading case was simulated where the external convection coefficient was increased from 10 to 20 $W/(m^2K)$ and the thermal conductivity of the plastic housing was increased from 1 to 10 W/(mK).

Increased thermal conductivity. In order to increase the heat transfer inside the canister, the carbon bed could be replaced with another type of activated carbon which has better heat transfer properties. One could also introduce metal granulates or bars which is mixed into the carbon bed for better total thermal conductivity.

A loading case was simulated where the thermal conductivity of the carbon bed was increased from 0.1 to 10 W/(mK).

4.6 Optimization

In order to get a good model, it is important to optimize the model so that all model parameters are tuned until the model is good enough. In order to determine how good the model is, a total error function was created.

$$\text{TotalError} = \sum_i w_i \epsilon_i \tag{4.7}$$

where w_i is the weight for a particular error and ϵ_i is the particular error.

Three different errors are created which all are a sum of squares over every time step:

$$\epsilon_i = \sum_t (\text{Measured} - \text{Simulated})^2 \tag{4.8}$$

The three errors used for optimization are the temperature at two normalized axial positions of the canister as well as the canister mass gain. The temperatures are important since it measures how far the adsorption front reached in the canister. The canister mass gain error is important since it is a measure of saturation and breakthrough which also ensures that the temperature profile in the canister does not only comes from thermal conductivity.

5
Results and discussion

The following chapter includes the experimental and simulated results. The experimental results for the loading and purging experiments as described in section 3.2 are presented. The simulations are then presented along with comparisons of the experiments. Lastly the simulated sensitivity analysis along with other important findings are presented.

5.1 Experimental results

The experimental results for all the experiments are presented below. First the results of the pressure drop are presented, thereafter the characteristics of the canister mass is presented, and later the temperature measurements are presented. Lastly the canister orientation results are presented.

5.1.1 Pressure drop

Before any loading and purging experiments were done, the pressure drop over the two experimental canisters were measured for an airflow of up to 100 litres per minute. The temperature during these experiments was 21 °C. The pressure drop over the carbon bed for the two canisters can be seen in fig. 5.1. The figure shows a similar pressure drop for the two canisters. The pressure drop is close to linear with regard to flow rate with only a small quadratic shape.

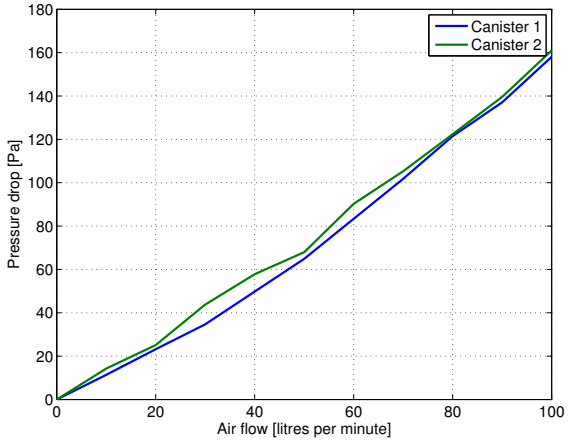

Figure 5.1: The pressure drop over the carbon bed for the two canisters.

5.1.2 Canister mass of the loading events

As described in section 3.2, six different loading experiments were carried out, labeled A through F. The different loading experiments are again described in table 5.1.

	Concentrations	
Butane flows	35 %	45%
36.5 g/h	Loading A	Loading B
70 g/h	Loading C	Loading D
100 g/h	Loading E	Loading F

Table 5.1: Loading experiments

The canister mass with regard to time for each experiment is presented in fig. 5.2. It can be seen that mass gain curve of case A and B have the lowest initial slope. This is expected since these cases refers to the slowest loading rate, where case C and D refers to an intermediate loading rate and case E and F is the fastest loading rate.

Comparing the cases with the same concentration (Case A, C, and E are the ones with a lower concentration. Case B, D, and F are the ones with a higher concentration), it can be seen that a lower concentration ends with a canister gain of approximately 95 grams while the cases with the higher concentration ends with approximately 110 grams. This result can be expected since a higher concentration yield a higher equilibrium loading, as mentioned in section 2.3.

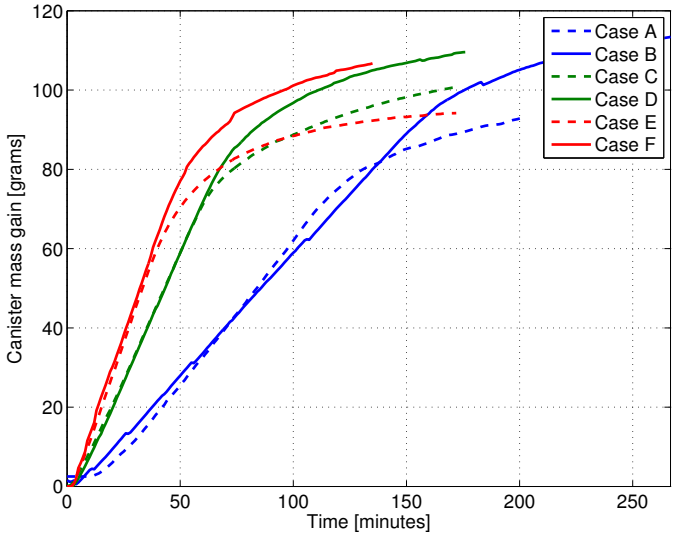

Figure 5.2: The canister mass gain for the loading events

5.1.3 Canister mass of the purging events

Three different purging flows were investigated as described in section 3.2 and these experiments are again described in table 5.2.

Air flow rate	Case label
9.14 LPM	Purge A
17.72 LPM	Purge B
25.20 LPM	Purge C

Table 5.2: Purging experiments

Figure 5.3 presents the three different purging flows. It can be seen that the first minutes are important for the purging performance where the canister releases a lot of butane. After ten minutes, the different flow rates make more difference than during the first minutes. It can be seen that a high flow rate purges the canister faster than a lower rate. Figure 5.3 also shows that the Purge B experiment possibly had a lower initial loading since it does not release the same mass as the other experiments, despite being the longest experiment.

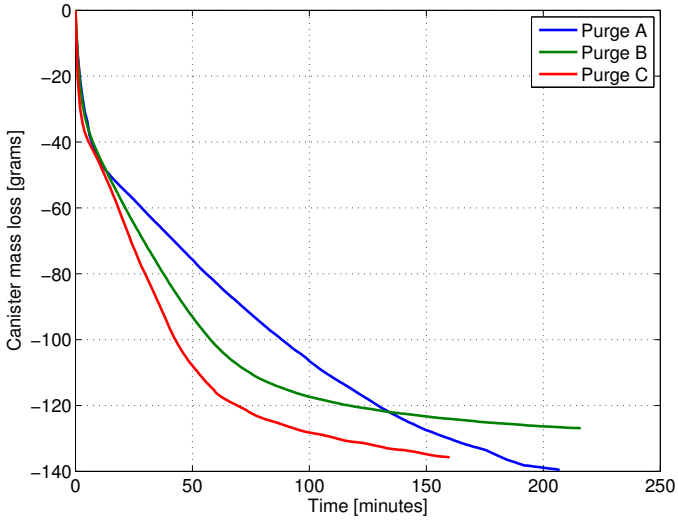

Figure 5.3: The canister mass loss for the purging events

5.1.4 Cumulative loading and purging

While fig. 5.2 and fig. 5.3 represent the transient data it can be hard to tell how efficient an event is, since the flow rates are very different. A way to represent this data instead is to scale the x-axis in order to represent the cumulative flow. This is simply done by multiplying the time with the flow rate for each data set. The result can be seen in fig. 5.4 where the loading events and the purging events are now plotted against the cumulative flow.

Figure 5.4a includes a help line which is a theoretical unlimited case where all cumulative flow is adsorbed. It is clear that a lower flow and a higher concentration is favourable since these lines are closer to the unlimited case.

Figure 5.4b shows that the desorption process is most efficient for the lowest flow for the first 200 litres. A linear desorption trend with regard to the cumulative flow, between 200 and 1000 litres purged, is observed regardless of flow rate.

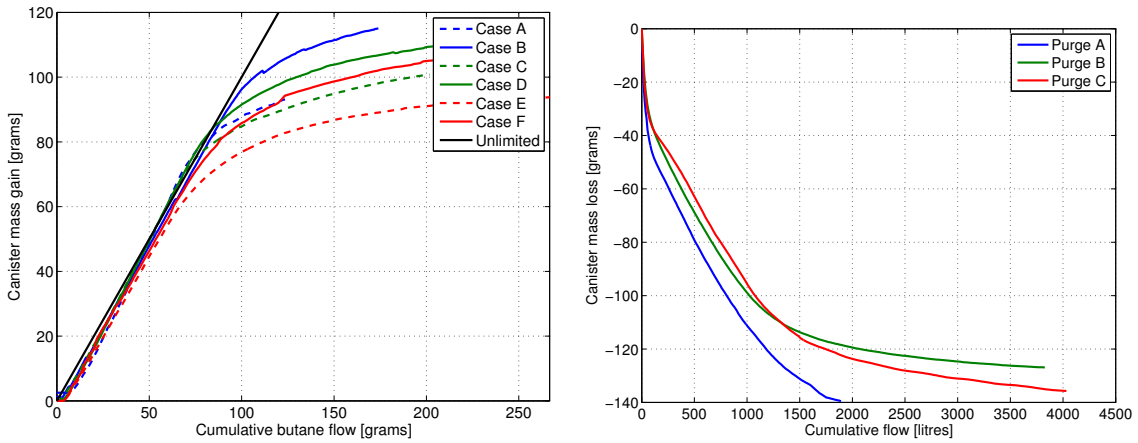

(a) Loading (b) Purging

Figure 5.4: Canister mass gain/loss with regard to the cumulative flow.

5.1.5 Temperature measurements for a loading event

The temperature of 20 different locations within the canister were recorded. In this section, the data for the first 120 minutes for loading case D is going to be looked at in detail. Figure 5.5 shows the six different thermocouples positioned in the radial center of the canister, labeled as their normalized axial position. The figure also shows the canister mass gain for the same period of time. In fig. 5.5 it can be seen that the temperature of the canister rapidly increases from the initial temperature, and later decreases more slowly. The temperature rises progressively axially in the canister and follows a clear trend. The last axial position, 0.884, does however decrease in temperature faster than the position before, 0.737, possibly due to cooling effects in the end of the canister.

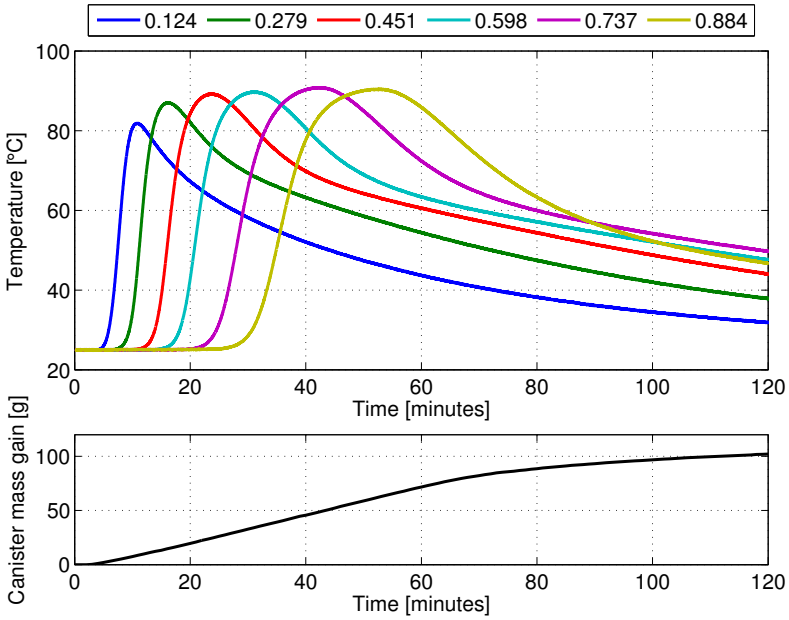

Figure 5.5: Mass gain and temperatures for loading case D

Figure 5.5 also includes the mass gain of the canister. The mass gain is linear and equal to the rate of 70 grams of n-butane per hour for the first 60 minutes. After 60 minutes the mass gain decreases and a breakthrough occurs.

Looking at the temperatures in the canister it can be noted that the breakthrough occurs at approximately the same time as when the temperature reaches its maximum value at the end of the canister. Hence it is reasonable to believe that a temperature rise is highly correlated to the position of the adsorption front.

Once a breakthrough has occurred after 60 minutes in fig. 5.5, the canister mass continues to rise as the temperature decreases. This can be explained with the non-isothermal effects explained in section 2.3.

5.1.6 Temperature measurements for a purging event

While the loading of the canister is an exothermic event which increases the temperature of the canister, the purging process is endothermic and thus decreases the temperature of the canister.

Figure 5.6 shows temperatures and mass loss for the purging process for purge case B. Note that the axial position still refers to the same positions as in the loading event, but the flow is reversed so that the incoming air comes in at an axial position of 1 while the air/butane mixture leaves the canister at axial position 0.

The figure shows a rapid temperature drop in the whole canister within the first minutes, along with a big mass loss implying a fast desorption process. The thermocouple closest to the inlet of the clean air, 0.884, quickly become heated to the ambient temperature possibly due to the convective heat transfer.

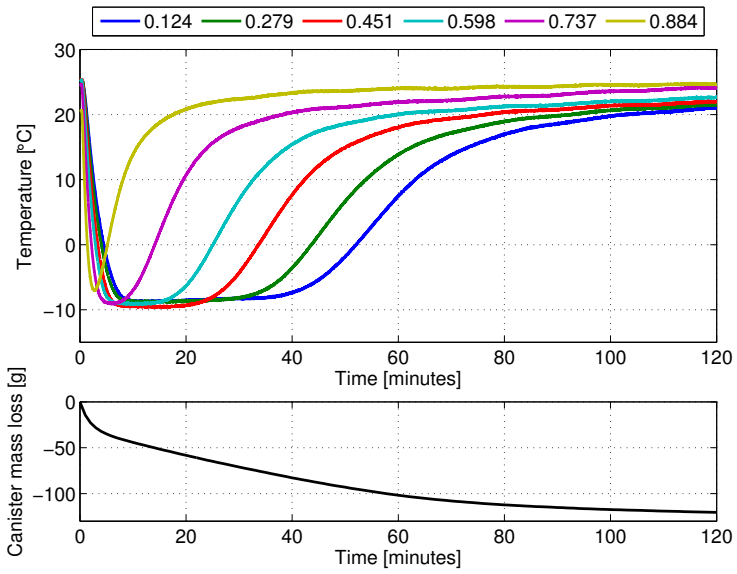

Figure 5.6: Temperature in the center of the canister, and the mass loss, for purge case B

Figure 5.6 also shows that the linear mass loss between 10 and 60 minutes decreases after 60 minutes as the temperature of the canister approaches the ambient temperature.

5.1.7 Can radial heat transfer be neglected?

One canister was prepared with 20 thermocouples in order to investigate radial heat transfer along with other phenomena. In the axial middle of the canister, three thermocouples were inserted to measure the temperature at three radial positions. The thermocouple positions are visualized in fig. 5.7 where the three normalized positions are indicated as well as the outer plastic housing of the canister.

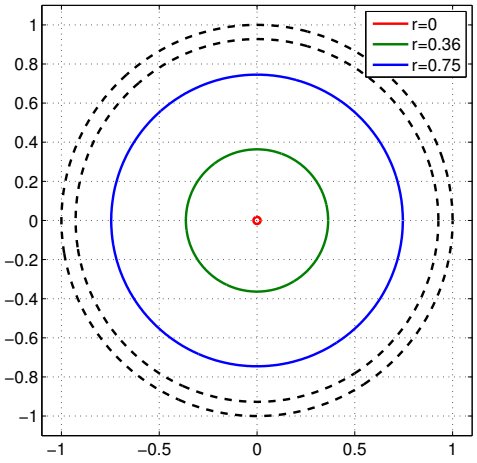

Figure 5.7: Thermocouples normalized position for measuring radial heat transfer

Figure 5.8 shows the temperatures at the canister middle axial position for a loading experiment D and the purging experiment B. The temperature is almost identical for the two thermocouples located closest to the canister middle, while a big deviation is seen for the thermocouple located at the outermost position. While the temperature deviates significantly, the characteristics of the temperature curves are all the same. Hence it is reasonable to believe that these phenomena exist because of radial heat transfer between the canister and the ambient air, rather than because of effects like dispersion and diffusion.

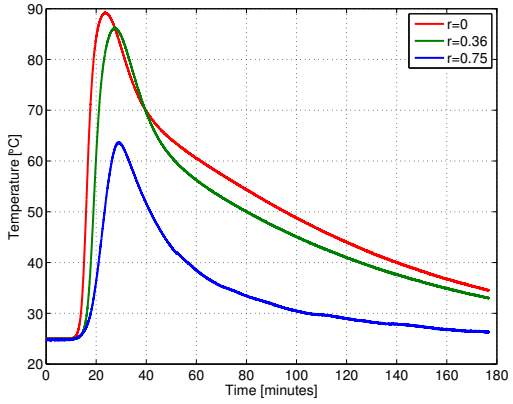

(a) Loading

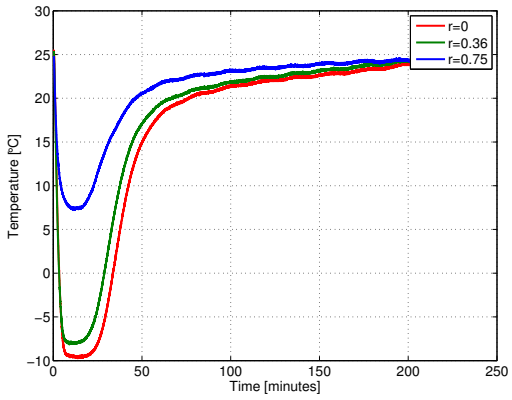

(b) Purging

Figure 5.8: Temperatures at the same axial position for the loading and purging event.

5.1.8 Canister orientation

As explained in section 3.1.3, the canister stood up on a balance so that the incoming loading flow is coming in from the bottom of the canister, and the breakthrough is exiting the canister from the top. Since n-butane (C_4H_{10}) has a molar mass of 58 grams per mole and nitrogen (N_2) has a molar mass of 28 grams per mole it can be expected that the gravitational effects will come into play when the canister is oriented horizontally instead of vertically.

In order to investigate this the canister was oriented horizontally and temperatures were compared between the vertical and horizontal orientation. Figure 5.9 compares the vertical orientation with the horizontal orientation. In fig. 5.9b the temperature sensor positions are shown and in fig. 5.9a a comparison between the vertical orientation and the horizontal orientation can be made. It is clear that in the vertical orientation, all temperature sensors have the same characteristics with the temperature differences explained in section 5.1.7. Figure 5.9a shows that a horizontal orientation of the canister changes these characteristics. Looking at the matching sensors between fig. 5.9b and fig. 5.9a makes it clear that a position closer to the ground experiences a temperature rise sooner than a position farther away from the ground.

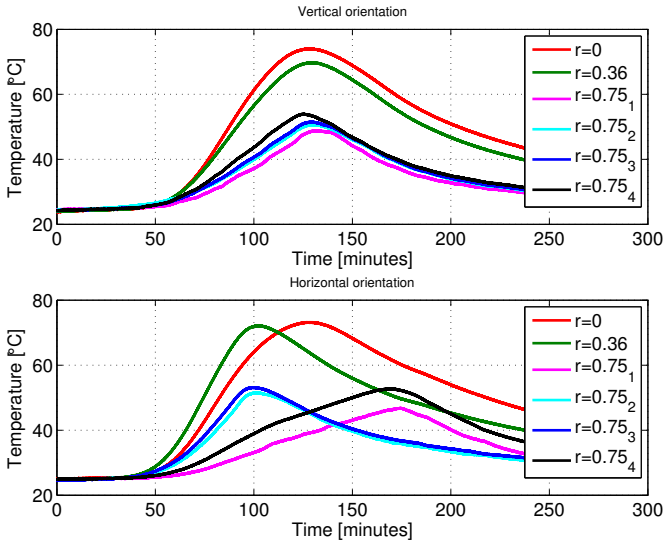

(a) Temperatures for the loading event

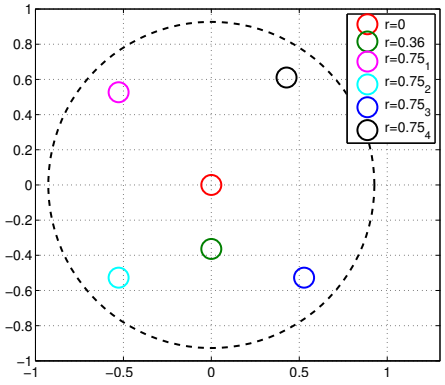

(b) Normalized temperature sensors positions

Figure 5.9: The loading event with a vertical and horizontal canister with labeled temperature position

Figure 5.9 makes it clear that the orientation of the canister influences the internal flow field. In all the other experiment in this thesis the canister was always oriented vertically in order to minimize these effects.

It should be noted that the loading events in this thesis differs from real life conditions as discussed in section 3.2 and hence it is hard to tell if the orientation in a car actually matters or not.

5.1.9 Measurement errors and inaccuracies

Measurements and experiments carried out in this thesis were made with far from ideal conditions. The flow rates of the loading and purging experiments were controlled using manually regulated rotameters which indicates the flow rate, and the reading of these rotameters can have influenced the results.

As a experimental canister were put on a balance, the pipe to the inlet as well as the thermocouples wires must be fixated in order to not influence the balance. This was hard to achieve which resulted in some discontinuities in the continuous balance logging when these pipes and wires changed position. An example can be seen in fig. 5.10 where the raw balance recording is shown. It is clear that between 50 and 100 minutes, fig. 5.10 shows two discontinuities where the mass gain rapidly jumps to a higher value. Filtering and adjustments were made to the data presented in this thesis in order to better represent a continuous balance logging without errors.

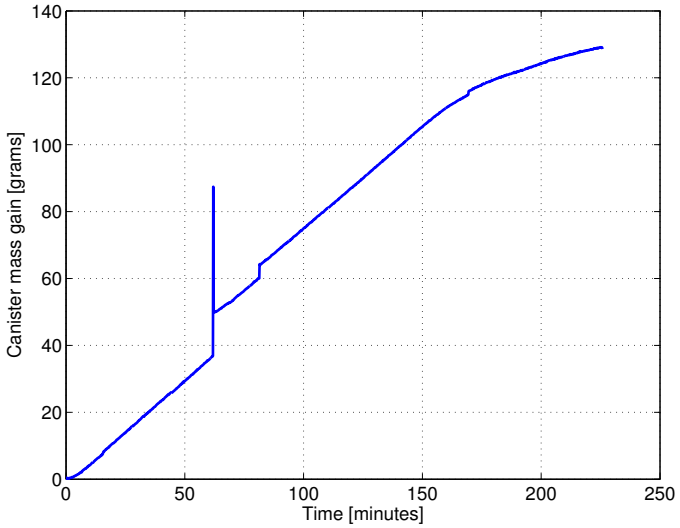

Figure 5.10: Balance recording of a loading experiment without any adjustments or filtering.

The temperature sensors normalized positions assumes that the carbon bed is perfectly cylindrical and that the plastic foam adds equal spacing at both sides of the carbon bed. Since the plastic foam can be deformed these assumption may be invalid and thus the normalized temperature sensors position can be slightly incorrect.

5.2 Simulations and comparisons with experimental results

The simulations were started with an optimization process for the pressure drop as well as for the chemical reactions. The results of the optimization process is first presented, and later the complete simulation results are presented.

5.2.1 Pressure drop optimization

First of all, the pressure drop was simulated in order to find the correct thickness of the walls in the `CatalystBrick` object. The wall thickness was found to be 0.45 mm for the cell density of 1 cell per mm^2. The results of the simulation along with the experimental results are shown in fig. 5.11. The figure shows that the simulated pressure drop is close to the experimental results with a deviation at higher flows.

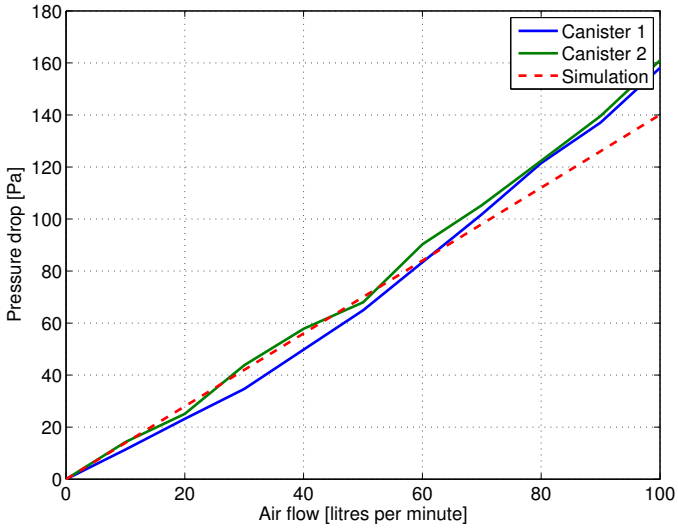

Figure 5.11: Simulation of the pressure drop along the experimental results

The pressure drop calculation in GT-Suite for the `CatalystBrick` brick object is calculated assuming a laminar flow within a monolith and using the simple relation between the Reynolds number and the friction factor for the laminar region.

One could possibly modify this behaviour using a Friction User Model in GT-Suite using the `UserCodeFReference` where a Fortran routine is called, but this was not investigated further since the pressure drop was good enough for the purging flow rates in this thesis.

5.2.2 Chemical reaction optimization

The heat of formation was set to $-145\,\mathrm{kJ/mol}$ which corresponds to a isosteric heat of adsorption of $-20\,\mathrm{kJ/mol}$ plus the heat of formation of n-butane of $-125\,\mathrm{kJ/mol}$. The heat of formation was reported by Pittam and Pilcher (1972) and the isosteric heat of adsorption was reported to be $-22.5\,\mathrm{kJ/mol}$ by Fiani et al. (2000).

Two different approaches for the chemical reactions have been discussed in this thesis; the Langmuir reaction expressions and the Dubinin-Astakhov isotherm with the LDF model.

Isothermic data for the n-butane adsorption onto Ingevity BAX1500 activated carbon was provided by Ingevity (Versen, 2016). The data contained three different temperatures, -10 °C , 25 °C and 80 °C and volumetric concentrations up to 50%. Both Langmuir isotherms as well as Dubinin-Astakhov (DA) isotherms were fitted to the data.

5.2.2.1 The Langmuir isotherm

Two attempts to fit the isotherm data according to the Langmuir isotherm were carried out. Figure 5.12 shows these Langmuir isotherm as well as the measured data for the three temperatures using an active site density of 3350 mol/m^3. The isotherms generally have a poor fit. This is likely explained with the few parameters used to describe the isotherm as described in section 2.3.1. Focusing on the 25 °C isotherm, fitting 1 have a better average fit while fitting 2 have a better fit at high concentrations. The parameters are presented in table 5.3

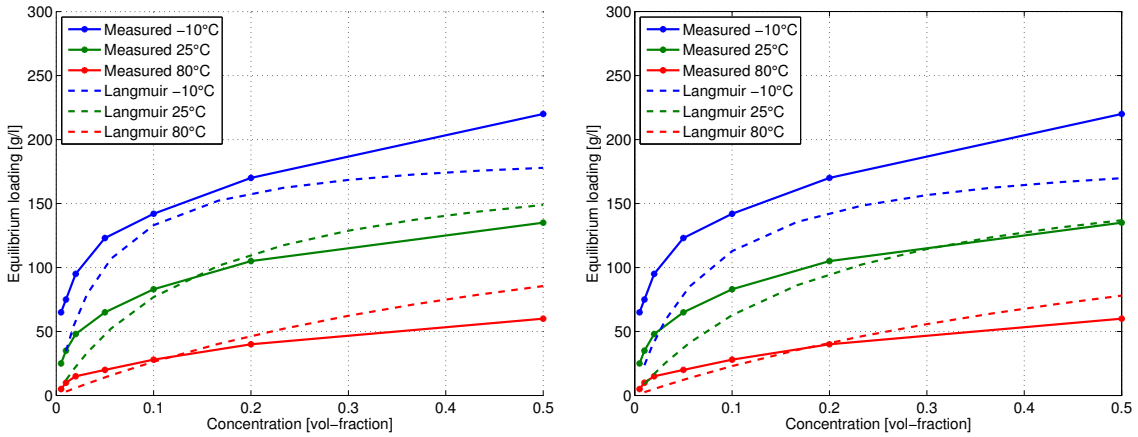

(a) Fitting 1 of the Langmuir isotherm

(b) Fitting 2 of the Langmuir isotherm

Figure 5.12: Langmuir isotherm equation fitting

Case	Langmuir fitting 1	Langmuir fitting 2
k_{ads}	$1 \times 10^3\,\mathrm{s}^{-1}$	$2 \times 10^3\,\mathrm{s}^{-1}$
k_{des}	$2 \times 10^7\,\mathrm{mol/(m^3 s)}$	$2 \times 10^7\,\mathrm{mol/(m^3 s)}$
E_A	20 000 J/(molK)	17 500 J/(molK)

Table 5.3: The parameters used for the Langmuir isotherm fitting

5.2.2.2 The Dubinin-Astakhov isotherm

The Dubinin-Astakhov isotherm has more flexibility and thus it can be expected that the isotherm is better for describing measured data. The parameters in the

Dubinin-Astakhov isotherm were tuned in order to fit the 25 °C measurements. The equation used were eq. (2.11) which do not have any temperature correction, but still takes the temperature into account in the adsorption potential.

Figure 5.13a shows the result of this fitting procedure. It is clear that the isotherm is almost identical to measurements for the 25 °C isotherm, but deviates for the other temperatures. This could likely be corrected with a temperature correction factor as eq. (2.12).

An attempt was made where the saturation (equilibrium) vapor pressure was fixed in order to limit the thermal effects. This fixation of the equilibrium vapor pressure turned out to be be a good correction for the temperature deviation previously discussed. Figure 5.13b shows the result of this isotherm equation. The resulting equation predicts the equilibrium loading well for all three temperatures, with only a small deviation at the lowest temperature and the highest concentration.

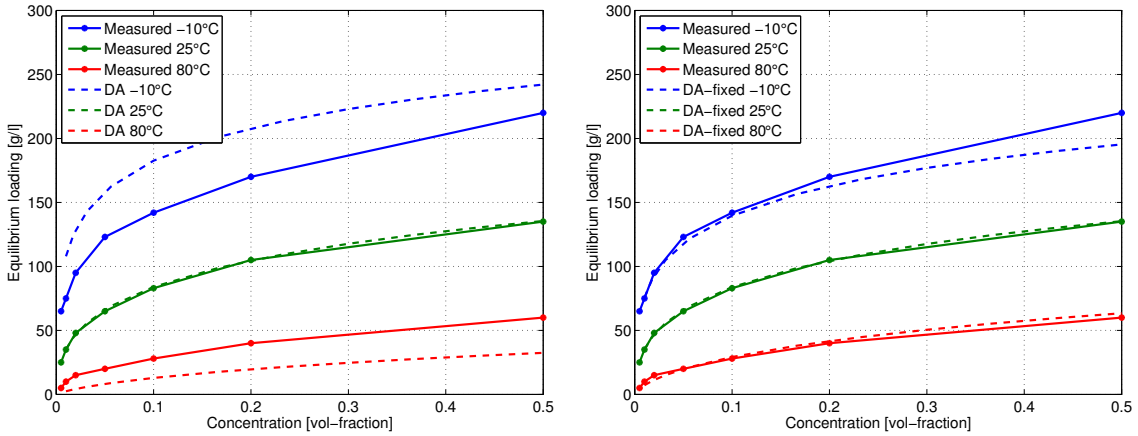

(a) Fitting of the Dubinin-Astakhov isotherm with $p_i^* = p_i^*(T)$

(b) Fitting of the Dubinin-Astakhov isotherm with $p_i^* = p_i^*(25\,^\circ\mathrm{C})$

Figure 5.13: Dubinin-Astakhov isotherm equation fitting

The Dubinin-Astakhov isotherm parameters, W_0, E and n are presented in table 5.4.

Parameter	**Value**
W_0	$462.29\,\mathrm{g/l_{carbon}}$
E	$30\,179.39\,\mathrm{J/mol}$
n	2.84

Table 5.4: Parameters found for the Dubinin-Astakhov isotherm

The only unknown parameter is the LDF time constant where the value of 0.02 (moles per second per moles of active sites) is found to be working well both for adsorption and desorption. This parameter value was arrived at from optimization and is discussed in more detail in section 5.4.

5.2.2.3 Choosing the isotherm equation for simulations

Simulations were run with both the Langmuir model (with parameters defined in table 5.3 as "Langmuir fitting 2") and the Dubinin-Astakhov LDF model (with a constant equilibrium vapor pressure) in order to determine which model preforms best.

The Langmuir model generally preforms well during loading but poorly during puring where the simulated process is too fast. A comparison for loading case B and purging case B can be seen in fig. 5.14. The models compared for the loading event in fig. 5.14a are close to identical. The models compared for the purging event in fig. 5.14b shows that the Langmuir model significantly over predicts the purging process.

The Dubinin-Astakhov isotherm LDF model, with a fixed saturation vapor pressure, preforms well both for loading and purging. This model was hence used for all the results presented in the latter sections. Thermal parameters that were optimized are found in table 4.2.

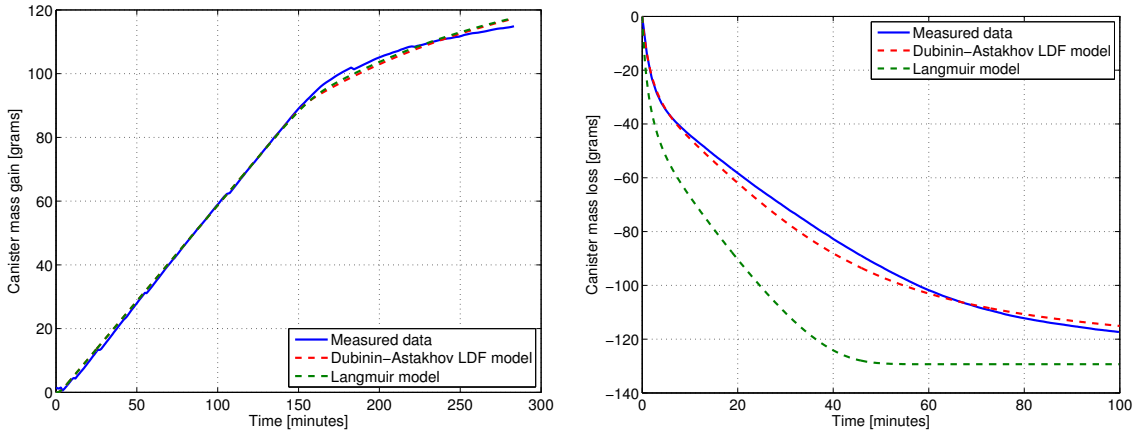

(a) Loading case B

(b) Purging case B

Figure 5.14: A comparison between the measured data, the Langmuir model and the Dubinin-Astakhov LDF model

5.2.3 Loading

The loading of the canister was simulated and compared with the experimental results. The simulations of loading case A through F can be seen in fig. 5.15. In general, the simulations predict the characteristics well but all cases with the lower concentration (Case A, C and E) they over predict the canister mass gain slightly.

Further in this section and in the sensitivity analysis the loading case B is looked at in more detail. Looking at the temperatures for case B, the temperature are compared with experiments at two different axial normalized positions; position 0.279 and position 0.737. As can be seen in fig. 5.16b the first position shows the same characteristics both in the simulation and in the experiment. For the second location, there is a small delay between the simulation and the experiment regarding time for the maximum temperature. Regardless of position, the simulation predicts

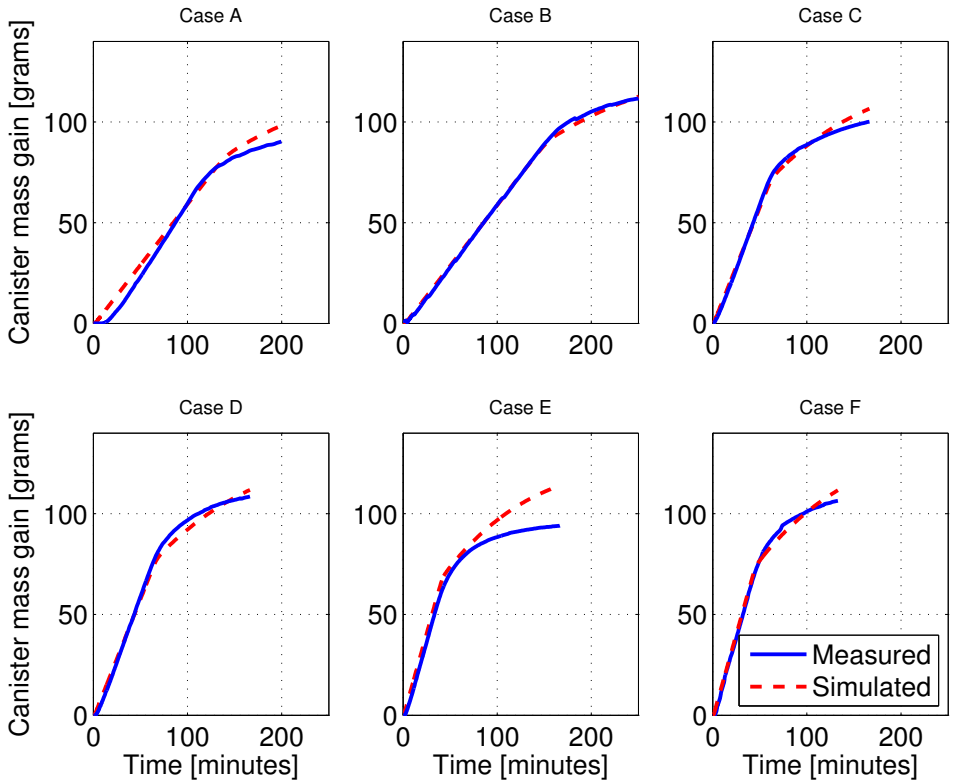

Figure 5.15: Simulation of the loading experiments

a lower temperature for the loading event than what is present during the experiment. This is not considered a problem since the simulation have a homogeneous temperature for every cell in the discretized canister. A homogeneous temperature should be lower than the measured temperature at the center of the bed as previously could be seen in fig. 5.8.

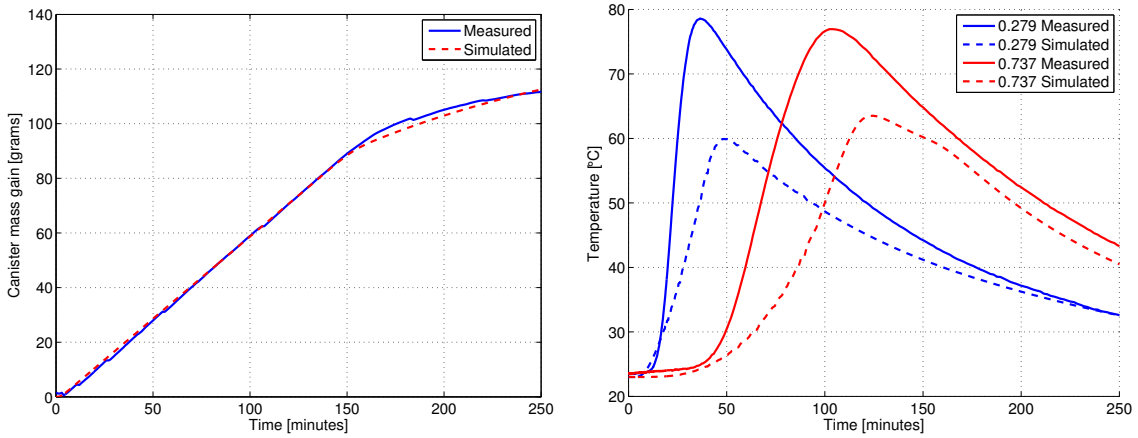

(a) The simulated and measured weight gain for the canister.

(b) The simulated and measured temperature at two axial positions of the canister.

Figure 5.16: Simulation and measurements of the temperature and weight gain during case B loading experiment.

5.2.4 Purging

For the purging events, the three different purging rates are simulated. In fig. 5.17 the simulation of all three purging rates can be seen as well as the measured data. The simulations all correspond well to the measured data. As for the loading event, one case will be presented in more detail. For the purging event, this is purge case B.

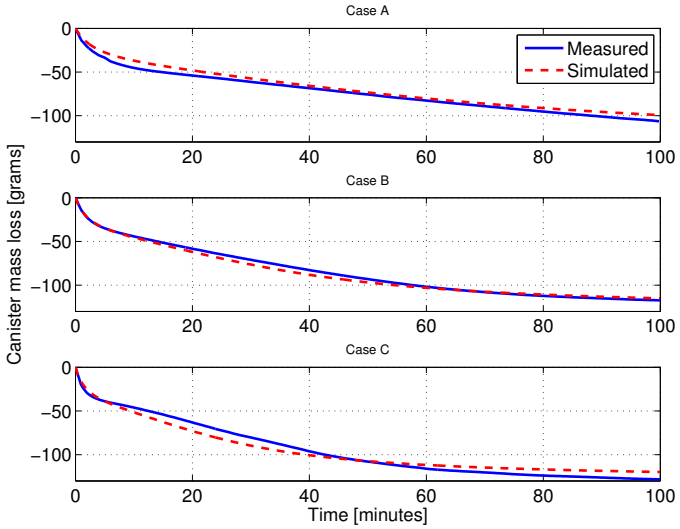

Figure 5.17: Simulation of the purging experiments

A detailed comparison between the simulated and measured data for purge case B is seen in fig. 5.18 where the mass loss as well as the temperature for the same two axial positions as before, are looked into with more detail. Figure 5.18b shows that the simulation predicts the same characteristics as the measured data regarding temperature, but just like in the loading case the temperature difference with regard to the ambient temperature is less extreme.

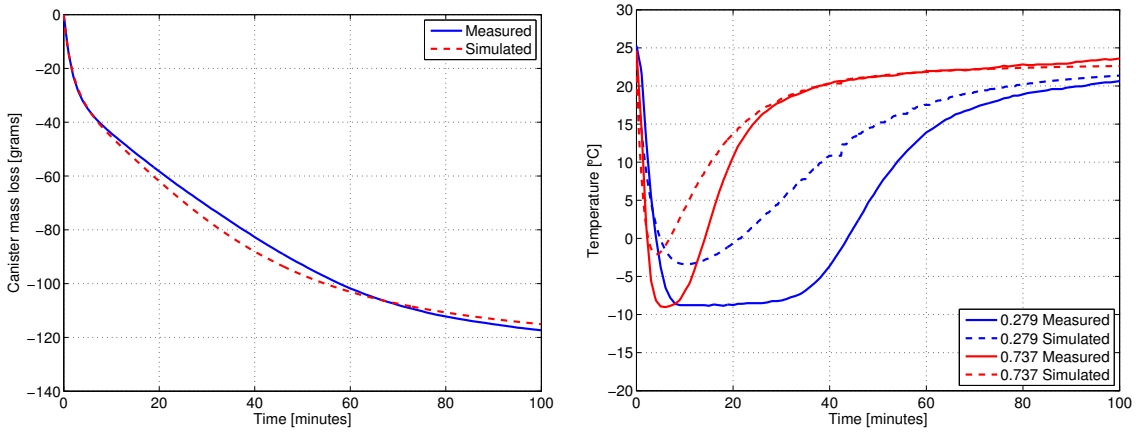

(a) Canister mass loss

(b) Temperature variations

Figure 5.18: Simulation and measurements of purge case B.

5.3 Sensitivity analysis

Once a good model was obtained which simulated loading and purging well, a simulation sensitivity analysis was carried out as described in section 4.5.

5.3.1 Length/Diameter ratio

The length/diameter ratio was changed according to section 4.5 and the loading event was investigated. The results of the mass gain for the different geometries are shown in fig. 5.19a. It can be seen that a higher length/diameter ratio yielded a more ideal canister and hence a later breakthrough. The sensitivity analysis does however show that the differences are small. In fig. 5.19b the simulated carbon bed energy loss is plotted for the three cases. As expected, a larger length/diameter ratio means that more energy could be released to the surroundings, making the canister behave more ideally. This is expected since the surface area increases as the length/diameter ratio increases. For purging, the length/diameter ratio again had no significant influence on performance.

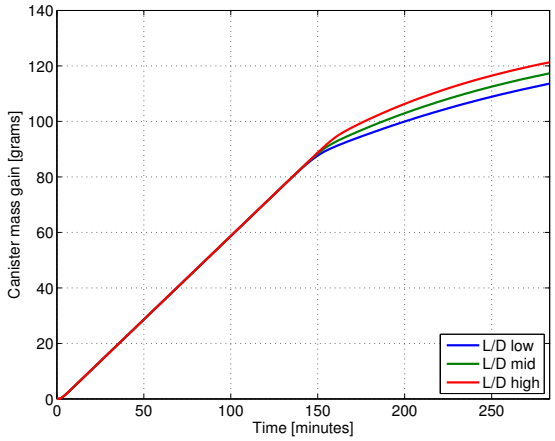

(a) The canister mass gain with different L/D.

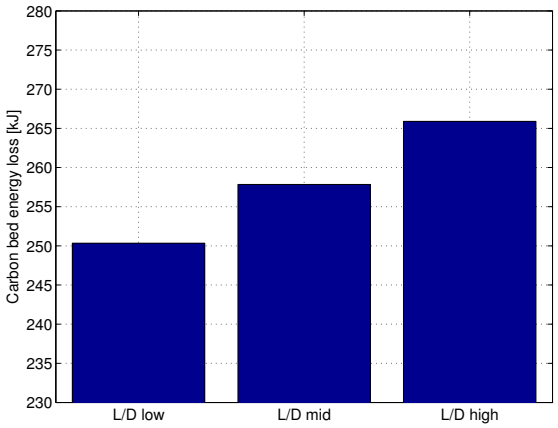

(b) The cumulative carbon bed energy loss for different L/D.

Figure 5.19: The simulated sensitivity analysis with respect to different length/diameter ratios.

The pressure drop was simulated as well and as expected, the pressure drop increases with increasing length/diameter ratio as shown in table 5.5.

Case	Pressure drop
L/D low	5.66 Pa
L/D mid	12.8 Pa
L/D high	29.0 Pa

Table 5.5: Simulation of the average pressure drop over the canister using a constant purging flow.

5.3.2 Heating of purge gases

Simulations were made where the incoming temperature of the purge flow was varied. The three temperatures are 23 °C , 45 °C and 70 °C at the constant incoming flow rate of 9.14 litres of nitrogen per minute. The mass loss for these temperatures can be seen in fig. 5.20 and while the shape of these curves look similar, the result of purging a fixed amount can be seen in table 5.6. An increased temperature to 70 °C reduces the time to purge 70 gram to just a third of the time at 23 °C .

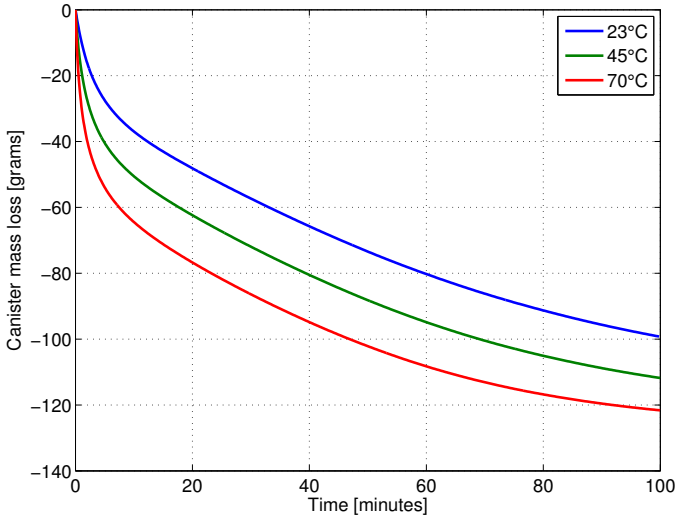

Figure 5.20: Simulation of a purging event using different incoming temperatures.

Temperature	Time to purge 70 grams
23 °C	45 minutes
45 °C	28 minutes
70 °C	14 minutes

Table 5.6: Simulation of the purging time using a constant purging flow.

5.3.3 Increased Internal and external heat transfer

One simulation was made where the *internal* heat transfer was increased, and one simulation was carried out where the *external* heat transfer was increased, as explained in section 4.5.2. The mass gain during loading for a constant loading of 45% n-butane at 36.5 g/h as well as the temperature simulated at the axial position of 0.279 can be seen in fig. 5.21a and fig. 5.21b.

The characteristics of an increased external heat transfer is quite straight forward looking at fig. 5.21; the temperature is always a bit lower and hence the canister behaves more ideally, giving a slightly better canister mass gain curve.

The characteristics of the increased internal heat transfer is however a bit more difficult to interpreter. Looking at fig. 5.21b it is clear that the temperature gain is not as extreme due to heat carried away due to axial internal heat transfer. It seems

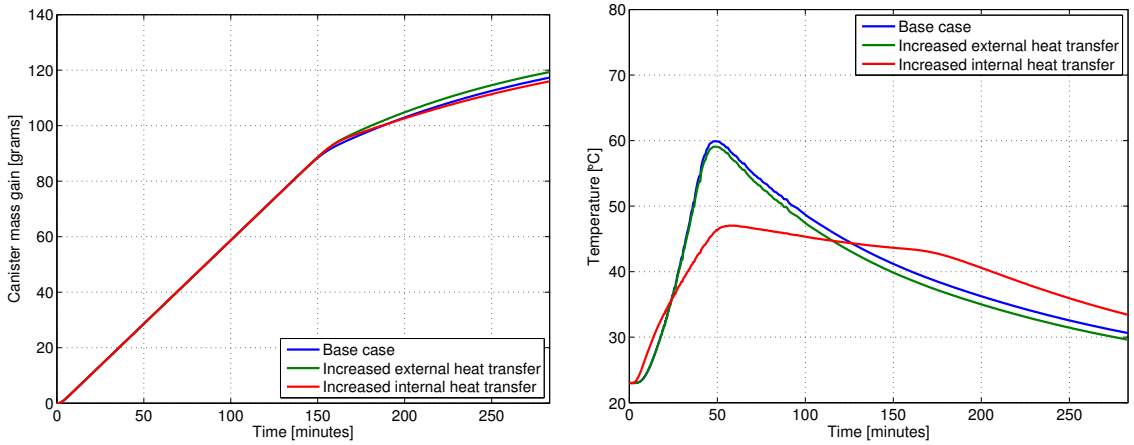

(a) Canister mass gain for the heat transfer sensitivity analysis

(b) Canister temperature at axial position 0.279.

Figure 5.21: Sensitivity analysis of an increased internal and external heat transfer.

like the canister does not however carry away the heat better to the surroundings than in the base case. The carbon bed is more homogeneous when it comes to temperature, but it does not perform significantly better than the improvement of better external heat transfer nor the base case.

5.3.4 Discretization length

A test was made in order to see if the discretization length of the canister made any difference. The discretization length was changed from 5 mm to 3 mm. The resulting change in canister mass gain at the end of a loading event was only 0.14% while the change in mass loss at the end of a purging event only was 0.92%.

A poorly discretized carbon bed would smear out the rapid temperature effects seen in both the purging and loading experiments.

5.4 The LDF time constant, internal mass transport and non constant purge flow

The LDF time constant was after optimization set to 0.02 moles per second per moles of active sites as previously mentioned. A sensitivity analysis for a loading and a purging experiment with different LDF time constants can be seen in fig. 5.22. It is clear that the loading event is slow enough for the time constant to have a wide range of values with minor influence on the results. During the purging event, the lower value of the time constant limits the purging phenomenon during the first 10 minutes, hence a higher LDF constant is preferable.

The findings from the sensitivity analysis in fig. 5.22 shows that it is not clear if there is an upper limit for the time constant, but it is shown that the LDF constant limits the fast desorption in the case of purging.

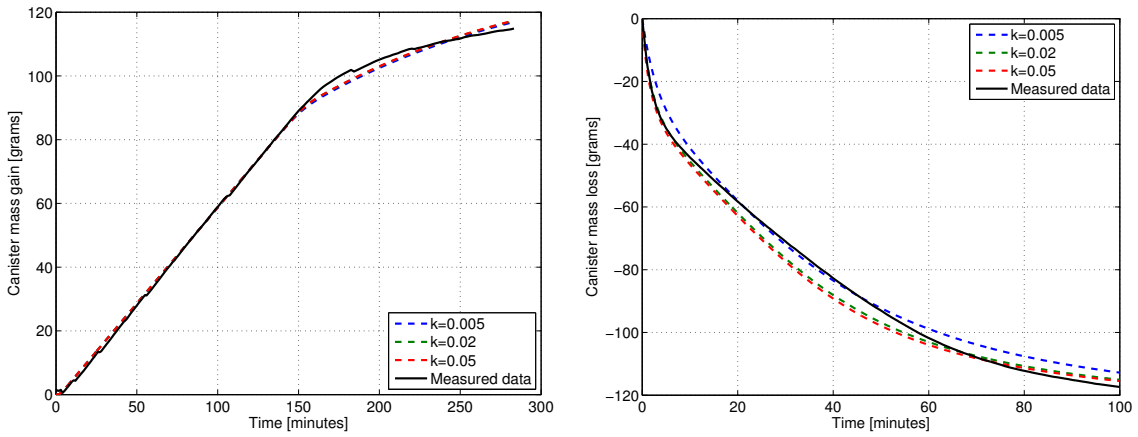

(a) Loading (b) Purging

Figure 5.22: The influence of changing the LDF time constant

The purging flows in this thesis have focused on constant flow rates, however as mentioned in section 2.1.2 the purging flow rate is varying in real life scenarios.

A simulation with a nonconstant purge flow rate was set up. The flow rate as well as the reaction rate for the axial position of 0.5 is shown in fig. 5.23 for the time constant of 0.02 moles per second per moles of active sites. The interesting part of this figure is what happens the moments after the purging flow is cut to zero. As can be seen in fig. 5.23 the reaction rate rapidly slows down but it takes about three seconds before the reaction rate is exactly zero. This means that it takes about three seconds for the carbon bed to stabilize to equilibrium.

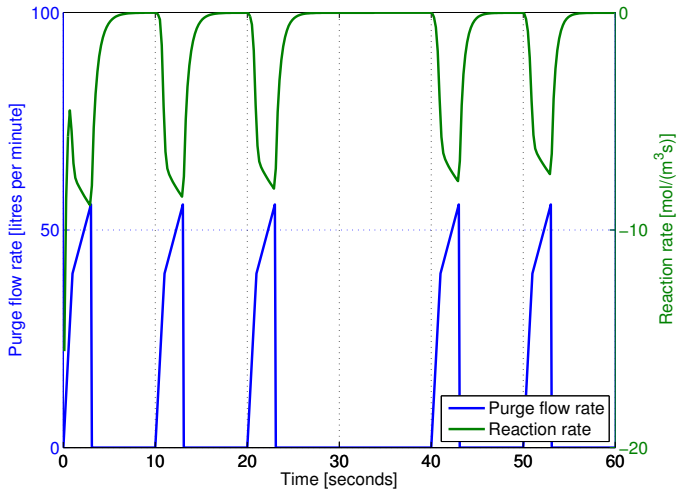

Figure 5.23: Simulation of a purging event with varying flow rate.

A large time constant means a faster reaction and a faster equilibrium, and in order to investigate the significance of this constant during the nonsteady flow, the two other time constants were simulated as well.

Figure 5.24 shows simulations where the time constant is varied. The figure shows two noteworthy phenomena. First of all the larger time constant results in

a larger reaction rate implying that more mass is released per second, despite the same (but dynamic) flow rate. Secondly it can be seen that the slow time constant results in that the reaction rate not reaching zero within the small windows between the purging events. When the window is bigger (between 23 and 40 seconds) the time is enough in order for the slowest time constant to reach equilibrium.

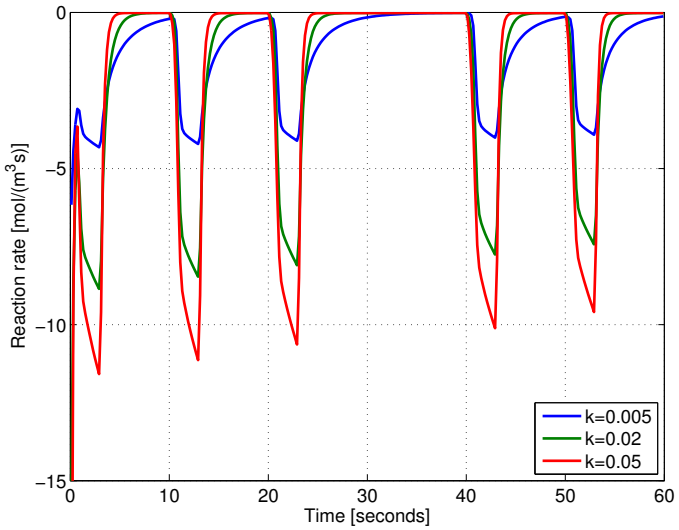

Figure 5.24: Simulation of a nonconstant purging event with different LDF time constants.

The simulations in fig. 5.24 have different reaction rates and hence different amounts of purged mass is released. As can be seen, the reaction rates spans from 4 to 11 $\mathrm{mol}/(\mathrm{m}^3\mathrm{s})$ when the maximum purge flow is sensed. With this model, the reaction rate can be extremely high when the purging flow is extremely high. The reason why the simulations showed in fig. 5.23 are similar for the purging event regardless of a LDF constant of 0.02 moles per second per moles of active sites or 0.05 moles per second per moles of active sites is because the adsorption process is, according to the simulation, always near equilibrium.

In theory there are several transport phenomena which can limit the adsorption and desorption, as described in section 2.2.2. Additional experiments using higher flow rates would be needed to verify an upper limit of the LDF time constant. If some limitation were to be simulated, the reaction rate could be limited as

$$r_{simulation} = \min(r_{calculated}, r_{limit}) \tag{5.1}$$

if the reaction rate is defined as a positive value.

6
Conclusions and future work

A one dimensional model of an activated carbon canister has been simulated and investigated in this project. The conclusion is that the model works well with the Linear Driving Force model with a Dubinin-Astkahov isotherm model with a fixed vapor saturation pressure. Effects such as radial heat transfer and canister orientation can influence the behaviour of the canister and these phenomena cannot be accounted for in a one dimensional model.

From the simulation sensitivity analysis it is clear that neither the length/diameter ratio, an increased external heat transfer, nor an increased internal heat transfer increased the performance significantly of the canister when loaded beyond breakthrough. With the model developed in this thesis, a high temperature of the purge flow significantly reduces the time or flow needed in order to purge the same amount as with a lower temperature.

Future work would be to verify experimental and simulation results for higher flow rates, such as ORVR loading and high flow rates during purging, and investigate if any mass transport limitation is present during these flow conditions. A verification of the simulation of the temperature purge flow sensitivity analysis would be of interest, and the temperature effects of possible mass transport limitations.

Future work can also include a two dimensional or three dimensional CFD model in order to better capture phenomena like radial heat transfer and detailed geometry. The flow field within the carbon bed and its characteristics with regards to phenomena like temperature gradients and viscosity gradients can be of interest.

One could also think about implementing the one dimensional canister model in another CAE application. If this application can be more flexible with regard to modelling parameters (such as the thermal properties in the carbon bed, which should be seen as functions of fractional coverage), a comparison would be interesting.

Bibliography

Bai, X., Isaac, K. M., Banerjee, R., Klein, D., Breig, W., & Oliver, L. (2004). *Modeling and Simulation of N-butane Adsorption/Desorption in a Carbon Canister*. SAE Technical Paper 2004-01-1680. doi:10.4271/2004-01-1680

Bansal, R. C. & Goyal, M. (2005). *Activated Carbon Adsorption*. ISBN: 978-0-8247-5344-3. Hoboken: CRC Press.

Chen, S. G. & Yang, R. T. (1994). Theoretical Basis for the Potential Theory Adsorption Isotherms. The Dubinin-Radushkevich and Dubinin-Astakhov Equations. *Langmuir*, *10*(11), 4244–4249. doi:10.1021/la00023a054

Derwent, R. G. (1995). Sources, distributions, and fates of VOCs in the atmosphere. In R. E. Hester & R. M. Harrison (Eds.), *Volatile organic compounds in the atmosphere* (Vol. 4, pp. 1–16). The Royal Society of Chemistry. doi:10.1039/9781847552310-00001

Do, D. (1997). Chapter 16. dynamics of adsorption in heterogeneous solids. In W. S. W. Rudziński & G. Zgrablich (Eds.), *Equilibria and dynamics of gas adsorption on heterogeneous solid surfaces* (Vol. 104, pp. 777–835). Studies in Surface Science and Catalysis. Elsevier. doi:10.1016/S0167-2991(97)80079-1

Do, D. (1998). *Adsorption Analysis: Equilibria and Kinetics*. Chemical Engineer Series, Volume 2. ISBN: 978-1-8609-4137-5. Imperial College Press.

Dubinin, M. (1975). Physical Adsorption of Gases and Vapors in Micropores. In J. D. D.A. Cadenhead & M. Rosenberg (Eds.), (Vol. 9, pp. 1–70). Progress in Surface and Membrane Science. Elsevier. doi:10.1016/B978-0-12-571809-7.50006-1

Fiani, E., Perier-Cambry, L., & Thomas, G. (2000). Non-isothermal Modelling of Hydrocarbon Adsorption on A Granulated Active Carbon. *Journal of Thermal Analysis and Calorimetry*, *60*(2), 557–570. doi:10.1023/A:1010147005169

Fiani, E., Perier-Camby, L., Thomas, G., & Sanalan, M. (1999). Calorimetric and Gravimetric Measurements of Hydrocarbon Adsorption on a Granulated Active Carbon. *Journal of Thermal Analysis and Calorimetry*, *56*(3), 1453–1459. doi:10.1023/A:1010139430558

Gamma Technologies. (2015). *GT-SUITE Exhaust Aftertreatment Application Manual*. Version 7.5.

Hall, F. J. (1965). Device for controlling the hydrocarbon evaporation losses from automotive vehicles. US Patent 319,158,7. Retrieved from http://patents.google.com/patent/US3191587A

Itakura, H., Kato, N., Kohama, T., Hyoudou, Y., & Murai, T. (2000). *Studies on Carbon Canester to Satisfy LEVII EVAP Regulations*. SAE Technical Paper 2000-01-0895. doi:10.4271/2000-01-0895

Jakubov, T. S. & Mainwaring, D. E. (2002). Modified Dubinin–Radushkevich / Dubinin–Astakhov Adsorption Equations. *Journal of Colloid and Interface Science*, *252*(2), 263–268. doi:10.1006/jcis.2002.8498

Johnson, P. J., Setsuda, D. J., & Williams, R. S. (1999). Activated Carbon for Automotive Applications. In T. D. Burchell (Ed.), *Carbon materials for advanced technologies* (Chap. 8, pp. 235–268). Amsterdam: Pergamon. doi:10.1016/b978-008042683-9/50010-8

Knaebel, K. S. (2008). Albright's chemical engineering handbook. In L. F. Albright (Ed.), (Chap. 14. Adsorption, pp. 1119–1171). CRC Press. doi:10.1201/9781420014389.ch14

Kuronuma, H., Masuda, S., Kobayashi, N., Sato, K., & Yamasaki, K. (2011). *Study on Diffusion Behavior of Evaporative Fuel Gas from Gasoline Carbon Canister in Consideration of Temperature-Dependence*. SAE Technical Paper 2011-32-0532. doi:10.4271/2011-32-0532

Lange, N. & Dean, J. (1973). *Lange's handbook of chemistry* (10th ed.). McGraw-Hill.

Lavoie, G. A., Johnson, P. J., & Hood, J. F. (1996, May). Carbon canister modeling for evaporative emissions: adsorption and thermal effects. In *Sae technical paper*. SAE International. doi:10.4271/961210

Lin, J.-S., Dong, M., Ali, S., Hipp, M., & Schnepper, C. (2012, April). Vehicular Emission Performance Simulation. In *Sae technical paper*. SAE International. doi:10.4271/2012-01-1059

Liu, H., Man, H., Tschantz, M., Wu, Y., He, K., & Hao, J. (2015). VOC from Vehicular Evaporation Emissions: Status and Control Strategy. *Environmental Science & Technology*, *49*(24), 14424–14431. PMID: 26599318. doi:10.1021/acs.est.5b04064

Mellios, G. & Samaras, Z. (2007). An empirical model for estimating evaporative hydrocarbon emissions from canister-equipped vehicles. *Fuel*, *86*(15), 2254–2261. doi:10.1016/j.fuel.2007.01.031

Pittam, D. A. & Pilcher, G. (1972). Measurements of heats of combustion by flame calorimetry. part 8.-methane, ethane, propane, n-butane and 2-methylpropane. *J. Chem. Soc., Faraday Trans. 1*, *68*, 2224–2229. doi:10.1039/F19726802224

Reddy, S. (2012). Understanding and Designing Automotive Evaporative Emission Control Systems. SAE Technical Paper 2012-01-1700. doi:10.4271/2012-01-1700

Sato, K. & Kobayashi, N. (2011). Adsorption and desorption simulation of carbon canister using n-butane as model compound of gasoline. *Journal of the Japan Petroleum Institute*, *54*(3), 136–145. doi:10.1627/jpi.54.136

Sato, K., Kobayashi, N., & Hasatani, M. (2009). Calculation Method of Adsorption and Desorption Performance of Butane Gas in Carbon Canister. *SAE International Journal of Engines*, *1*(1), 409. doi:10.4271/2008-01-0625

Smith, L., Hussain, A., Pautasso, E., Servetto, E., Graziano, E., & Brown, J. (2015). EVAP System Fluid-Dynamics and Chemistry Modelling for EMS Purge Control Development and Optimization. SIA Powertrain Conference, Versailles 2015. Retrieved from http://www.sia.fr/publications/109-evap-system-fluid-

dynamics-and-chemistry-modelling-for-ems-purge-control-development-and-optimization

Versen, E. (2016). Private Communication. Ingevity Corporation.

Williams, R. S. & Clontz, C. R. (2001). *Impact and Control of Canister Bleed Emissions*. SAE Technical Paper 2001-01-0733. doi:10.4271/2001-01-0733

Yamasaki, K., Suzuki, T., Sato, K., Kobayashi, N., Tanaka, H., & Endo, H. (2009, April). Analysis of butane diffusion in activated carbon canister. *SAE Int. J. Fuels Lubr. 2*, 455–461. doi:10.4271/2009-01-0976

Zaremba, A. T. & Jennings, M. (2011). Purge Modeling for New Propulsion System Technology Applications. *SAE International Journal of Engines*, *4*(1), 998–1006. doi:10.4271/2011-01-0858

A

Canister geometry

A detailed picture of the of the canister geometry is seen in fig. A.1. Note that proportions might not be according to scale.

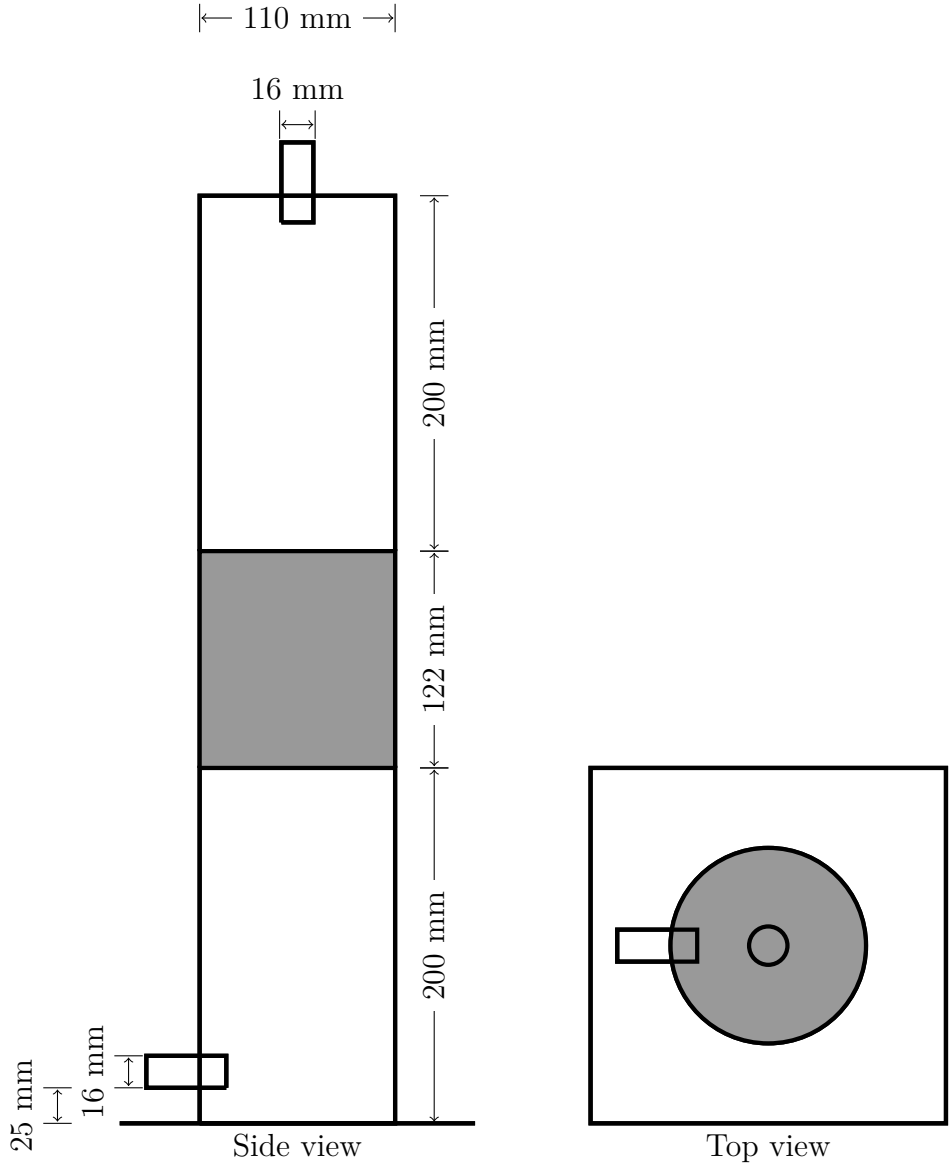

Figure A.1: Detailed sketch and measurements of the canister geometry

B

Temperature sensors positions

The temperature sensors positions for the two experimental canisters is presented in table B.1 and table B.2. θ refers to the tangential position, h refers to the height from the lower metal plate (the upper metal plate at a distance of 142 mm from the lower one), the depth is measured from the outer side of the plastic housing. The normalized axial position is calculated from the assumption that the carbon bed's height is 122.4 mm.

Sensor	θ	h (mm)	**Depth** (mm)	**Norm. axial position**
1	45	21.5	14	0.096
2	45	72	14	0.508
3	45	118	14	0.884
4	90	25	55	0.124
5	90	44	55	0.279
6	90	65	55	0.451
7	90	83	55	0.598
8	90	100	55	0.737
9	90	118	55	0.884
10	90	-84	55	-0.767
11	90	224	55	1.750
12	135	25	14	0.124
13	135	115	14	0.860
14	180	25	35	0.124
15	180	72	35	0.508
16	180	120	35	0.900
17	-135	22	14	0.100
18	-135	117	14	0.876
19	-35	23	14	0.108
20	-35	116	14	0.868

Table B.1: Temperature sensors positions for experimental canister 1.

Sensor	θ	h (mm)	**Depth** (mm)	**Norm. axial position**
21	70	-83	55	-0.758
22	70	24	55	0.116
23	70	42	55	0.263
24	70	60	55	0.410
25	70	80	55	0.574
26	70	97	55	0.712
27	70	115	55	0.860
28	70	225	55	1.758

Table B.2: Temperature sensors positions for experimental canister 2.